

*Supplementary Information for:*

**Bis-Monophospholyl Dysprosium Cation Showing Magnetic Hysteresis at 48 K**

Peter Evans, Daniel Reta, George F.S. Whitehead, Nicholas F. Chilton,\* and David P. Mills\*

*Department of Chemistry, School of Natural Sciences, The University of Manchester, Oxford Road, Manchester, M13 9PL, U.K.*

**Contents**

<b>1. Crystallography</b>	<b>S2</b>
<b>2. Molecular structure of [NEt<sub>3</sub>H][Al{OC(CF<sub>3</sub>)<sub>3</sub>}<sub>4</sub>]</b>	<b>S4</b>
<b>3. NMR spectroscopy</b>	<b>S5</b>
<b>4. ATR-IR spectroscopy</b>	<b>S7</b>
<b>5. Magnetic measurements</b>	<b>S8</b>
<b>6. CASSCF-SO electronic structure and <i>ab initio</i> spin dynamics</b>	<b>S20</b>
<b>7. References</b>	<b>S34</b>

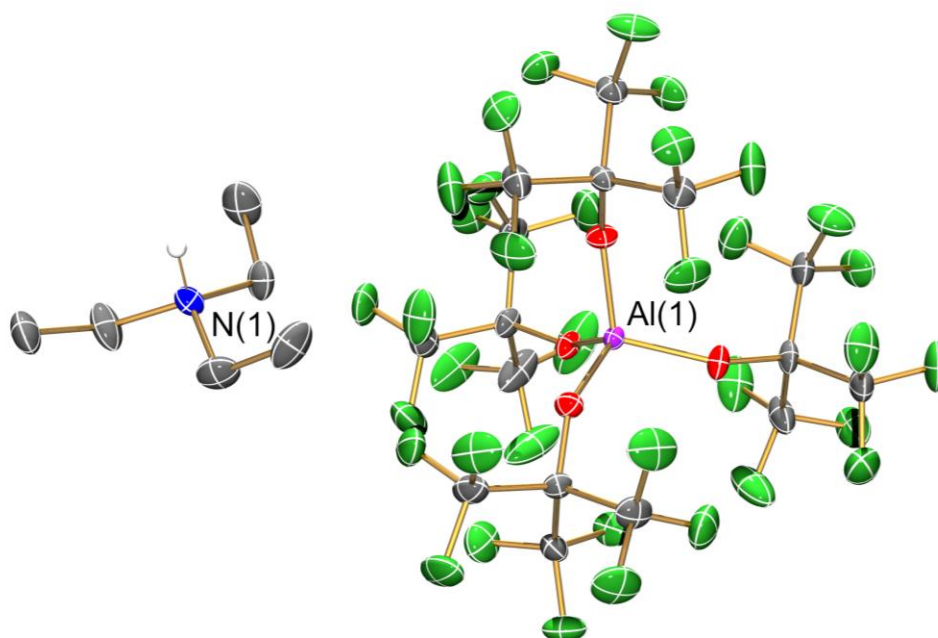
## 1. Crystallography

The crystal data for **1** and  $[\text{NEt}_3\text{H}][\text{Al}\{\text{OC}(\text{CF}_3)_3\}_4]$  are compiled in Table S1. Data for crystals of **1** were collected using a Rigaku Oxford Diffraction FR-X diffractometer with a HyPix 6000HE photon counting detector and VariMax<sup>TM</sup> micro focus optics with Cu K $\alpha$  radiation ( $\lambda = 1.54178 \text{ \AA}$ ). Crystals of  $[\text{NEt}_3\text{H}][\text{Al}\{\text{OC}(\text{CF}_3)_3\}_4]$  were examined using a Rigaku Oxford Diffraction Supernova diffractometer with a CCD area detector and micro focus optics with Mo K $\alpha$  radiation ( $\lambda = 0.71073 \text{ \AA}$ ). Intensities were integrated from data recorded on  $1^\circ$  frames by  $\omega$  rotation. Cell parameters were refined from the observed positions of all strong reflections in each data set. A multi-scan (**1**) or Gaussian grid face-indexed ( $[\text{NEt}_3\text{H}][\text{Al}\{\text{OC}(\text{CF}_3)_3\}_4]$ ) absorption correction with a beam profile was applied.<sup>1</sup> The initial structure was solved using ShelXT<sup>2</sup> and the model was refined by full-matrix least-squares on all unique  $F^2$  values using ShelXL,<sup>3</sup> with anisotropic displacement parameters for all non-hydrogen atoms, and with constrained riding hydrogen geometries;  $U_{\text{iso}}(\text{H})$  was set at 1.2 (1.5 for methyl groups) times  $U_{\text{eq}}$  of the parent atom. The largest features in final difference syntheses were close to heavy atoms and were of no chemical significance. CrysAlisPro<sup>1</sup> was used for control and integration, and SHELX<sup>2,3</sup> was employed through OLEX2<sup>4</sup> for structure solution and refinement. ORTEP-3<sup>5</sup> and POV-Ray<sup>6</sup> were employed for molecular graphics. CCDC 1957222 (**1**) and 1957223 ( $[\text{NEt}_3\text{H}][\text{Al}\{\text{OC}(\text{CF}_3)_3\}_4]$ ) contain the supplementary crystal data for this article. These data can be obtained free of charge from the Cambridge Crystallographic Data Centre via [www.ccdc.cam.ac.uk/data\\_request/cif](http://www.ccdc.cam.ac.uk/data_request/cif).

**Table S1.** Crystallographic data for **1** and [NEt<sub>3</sub>H][Al{OC(CF<sub>3</sub>)<sub>3</sub>}<sub>4</sub>].

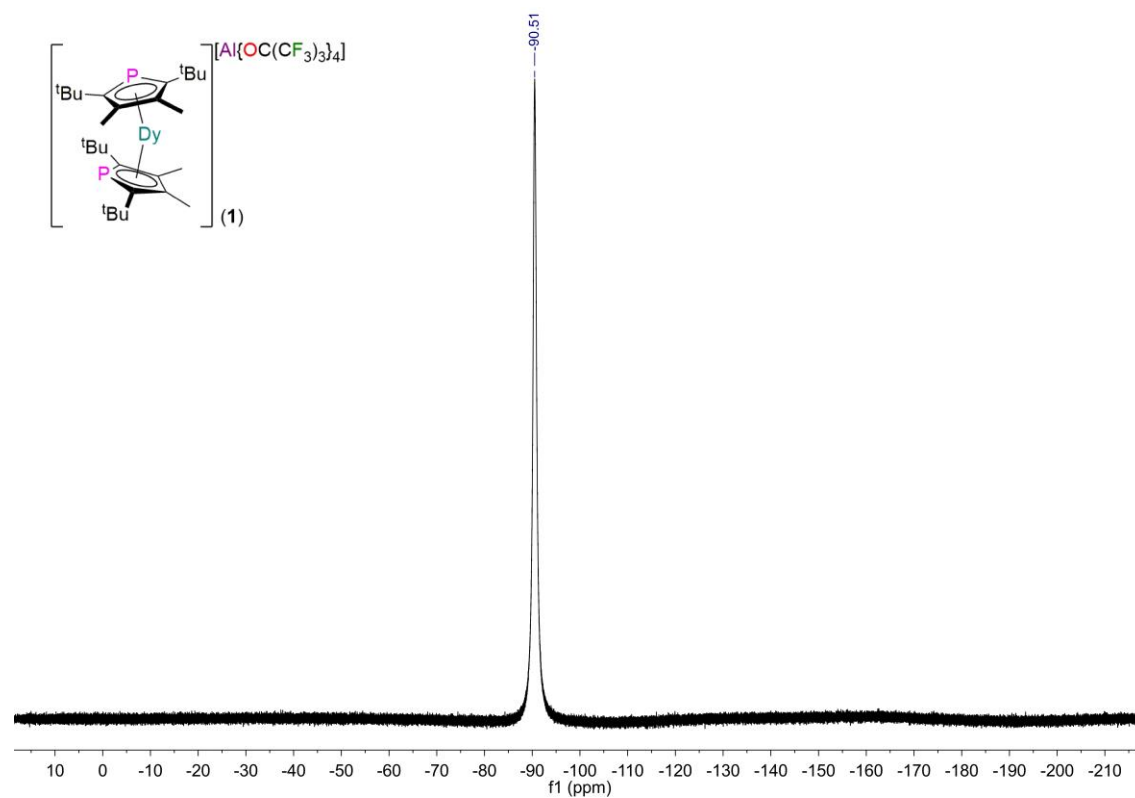
	<b>1</b>	[NEt <sub>3</sub> H][Al{OC(CF <sub>3</sub> ) <sub>3</sub> } <sub>4</sub> ]
Empirical formula	C <sub>44</sub> H <sub>48</sub> AlDyF <sub>36</sub> O <sub>4</sub> P <sub>2</sub>	C <sub>22</sub> H <sub>16</sub> AlF <sub>36</sub> N
Formula weight	1576.24	1069.34
Temperature/K	100.00(10)	150(3)
Crystal system	monoclinic	monoclinic
Space group	P2 <sub>1</sub> /c	P2 <sub>1</sub> /c
a/Å	17.3855(2)	9.6234(4)
b/Å	10.76015(13)	25.2268(9)
c/Å	31.9194(4)	14.7614(5)
α/°	90	90
β/°	105.4590(13)	90.021(3)
γ/°	90	90
Volume/Å <sup>3</sup>	5755.14(13)	3583.6(2)
Z	4	4
ρ <sub>calc</sub> /g/cm <sup>3</sup>	1.819	1.982
μ/mm <sup>-1</sup>	9.092	0.271
F(000)	3108.0	2096.0
Crystal size/mm <sup>3</sup>	0.221 × 0.186 × 0.138	0.206 × 0.152 × 0.118
Radiation	CuKα (λ = 1.54184)	MoKα (λ = 0.71073)
2Θ range for data collection/°	5.75 to 152.67	4.25 to 50.70
Index ranges	-21 ≤ h ≤ 21, -13 ≤ k ≤ 13, -39 ≤ l ≤ 40	-11 ≤ h ≤ 11, -30 ≤ k ≤ 30, 0 ≤ l ≤ 17
Reflections collected	11832	6563
Independent reflections	10839 [R <sub>int</sub> = 0.0486, R <sub>sigma</sub> = 0.0319]	5457 [R <sub>int</sub> = 0.0645, R <sub>sigma</sub> = 0.0748]
Data/restraints/parameters	11832/583/929	6563/522/581
Goodness-of-fit on F <sup>2</sup>	1.020	0.995
Final R indexes [I >= 2σ (I)]	R <sub>1</sub> = 0.0379, wR <sub>2</sub> = 0.1002	R <sub>1</sub> = 0.0492, wR <sub>2</sub> = 0.1051
Final R indexes [all data]	R <sub>1</sub> = 0.0414, wR <sub>2</sub> = 0.1023	R <sub>1</sub> = 0.0630, wR <sub>2</sub> = 0.1147
Largest diff. peak/hole / e Å <sup>-3</sup>	0.98/-1.81	0.32/-0.37

## 2. Molecular structure of $[\text{NEt}_3\text{H}][\text{Al}\{\text{OC}(\text{CF}_3)_3\}_4]$

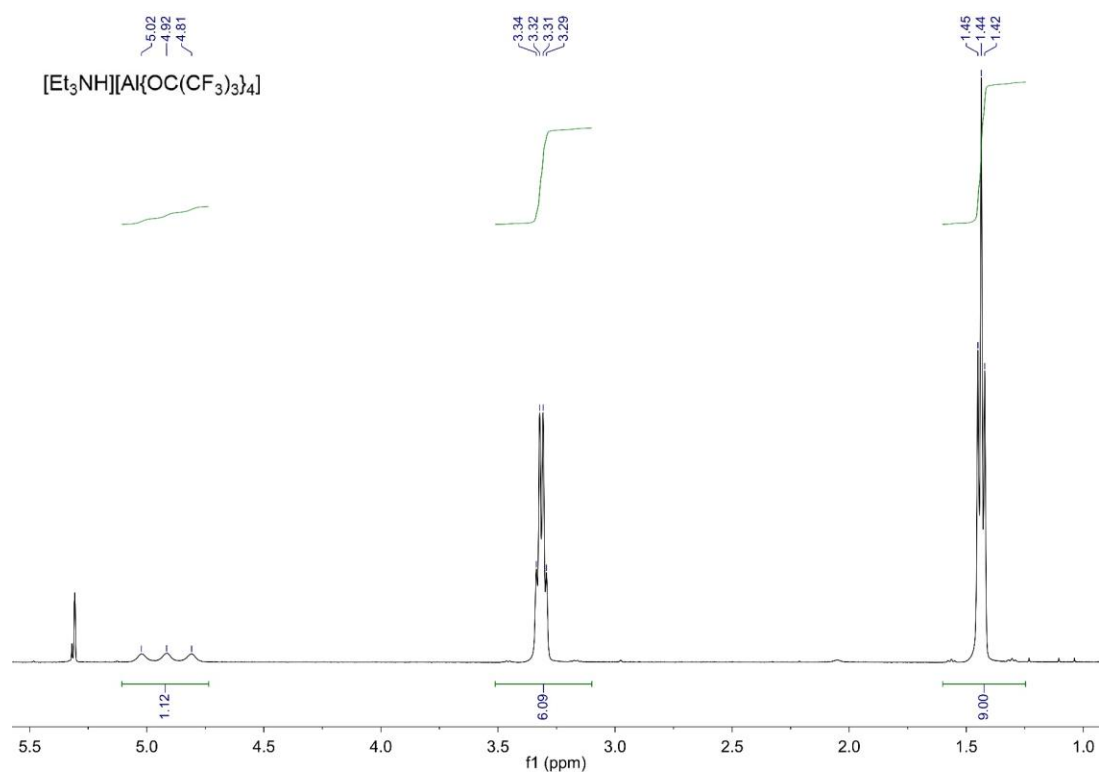


**Figure S1.** Molecular structure of  $[\text{NEt}_3\text{H}][\text{Al}\{\text{OC}(\text{CF}_3)_3\}_4]$  with selected atom labelling. Displacement ellipsoids set at 50% probability level, solvent of crystallization and hydrogen atoms apart from on N(1) are omitted for clarity. C atoms are grey, O atoms are red and F atoms are green.

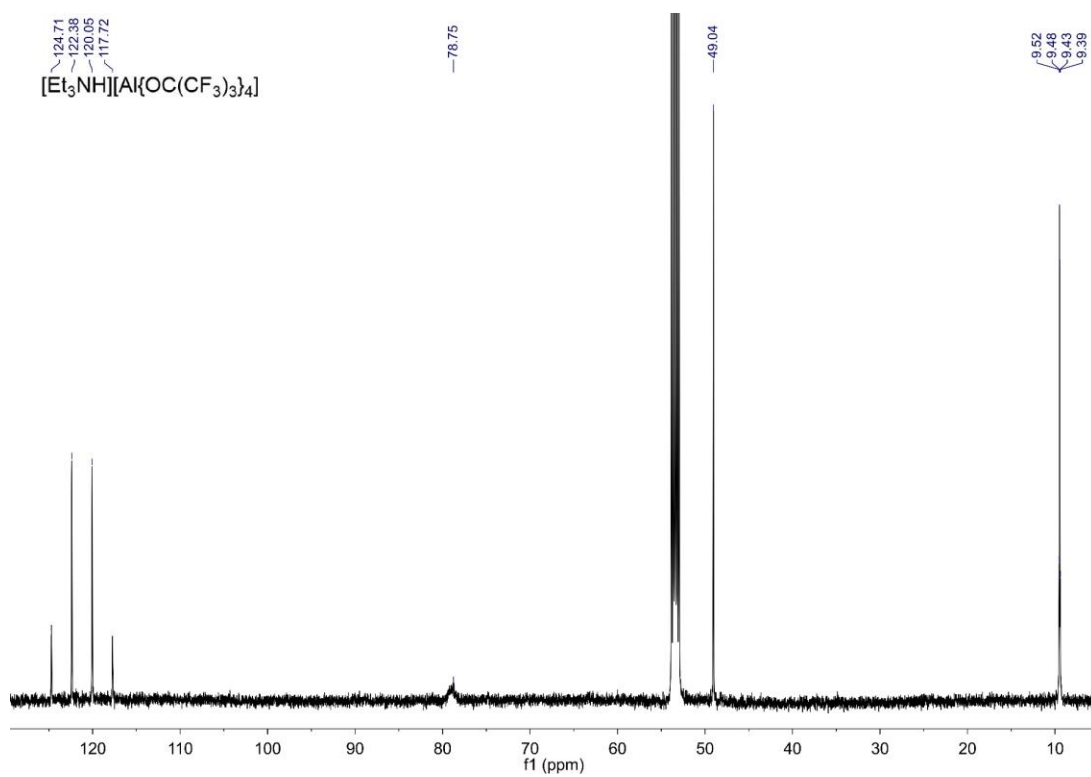
### 3. NMR Spectroscopy



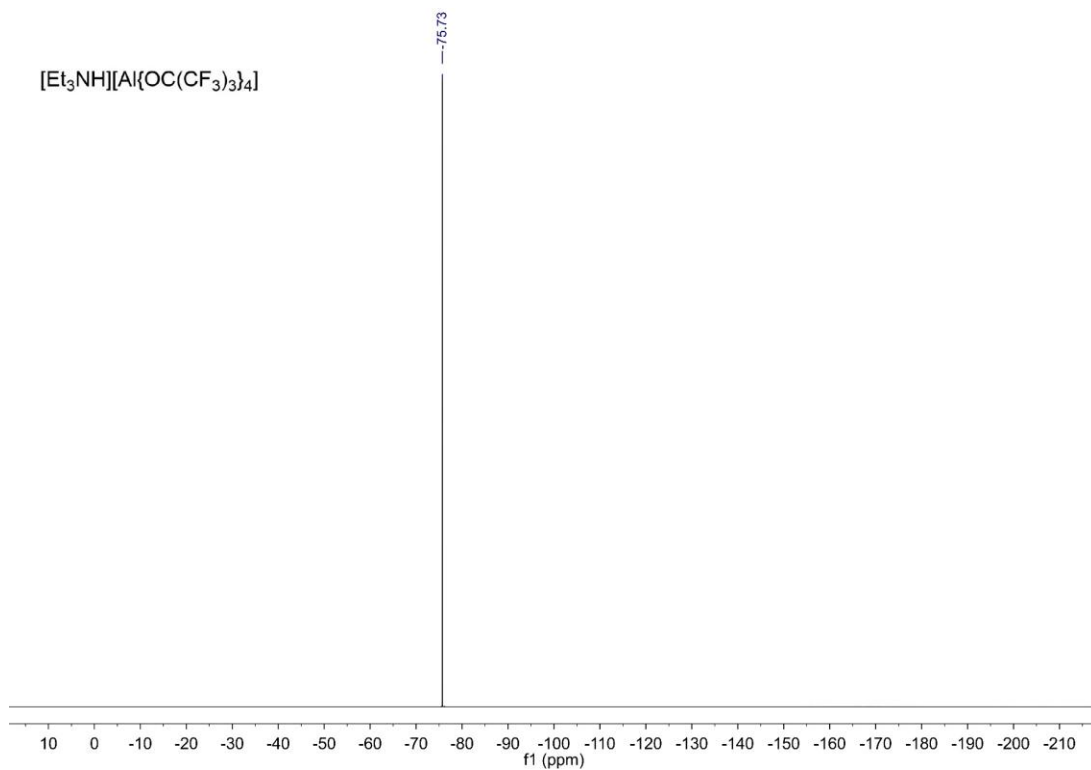
**Figure S2.**  $^{19}\text{F}$  NMR spectrum of **1** in  $\text{C}_6\text{D}_5\text{Cl}$ .



**Figure S3.**  $^1\text{H}$  NMR spectrum of  $[\text{NEt}_3\text{H}][\text{Al}(\text{OC}(\text{CF}_3)_3)_4]$  in  $\text{CD}_2\text{Cl}_2$ .

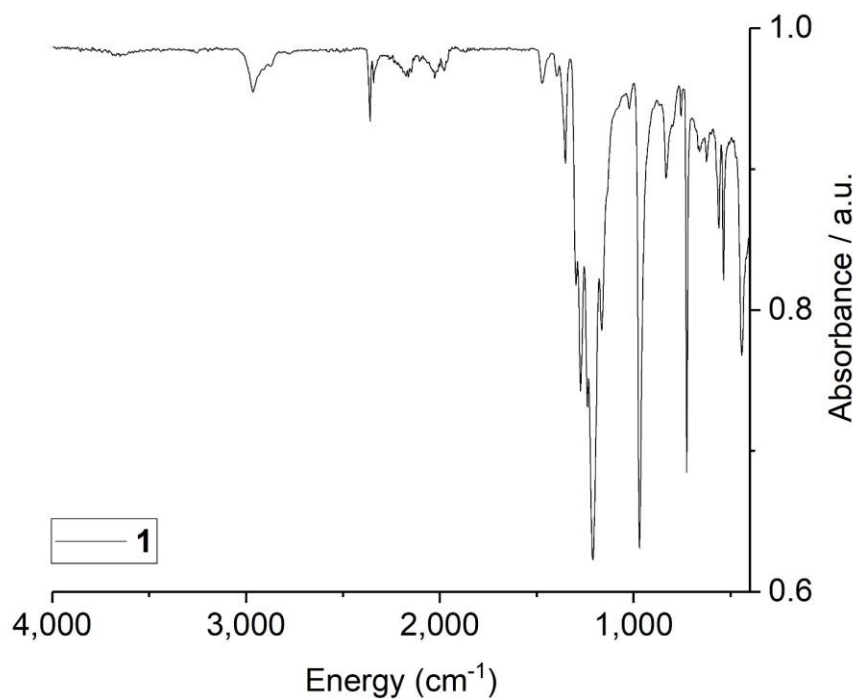


**Figure S4.**  $^{13}\text{C}$  NMR spectrum of  $[\text{NEt}_3\text{H}][\text{Al}\{\text{OC}(\text{CF}_3)_3\}_4]$  in  $\text{CD}_2\text{Cl}_2$ .

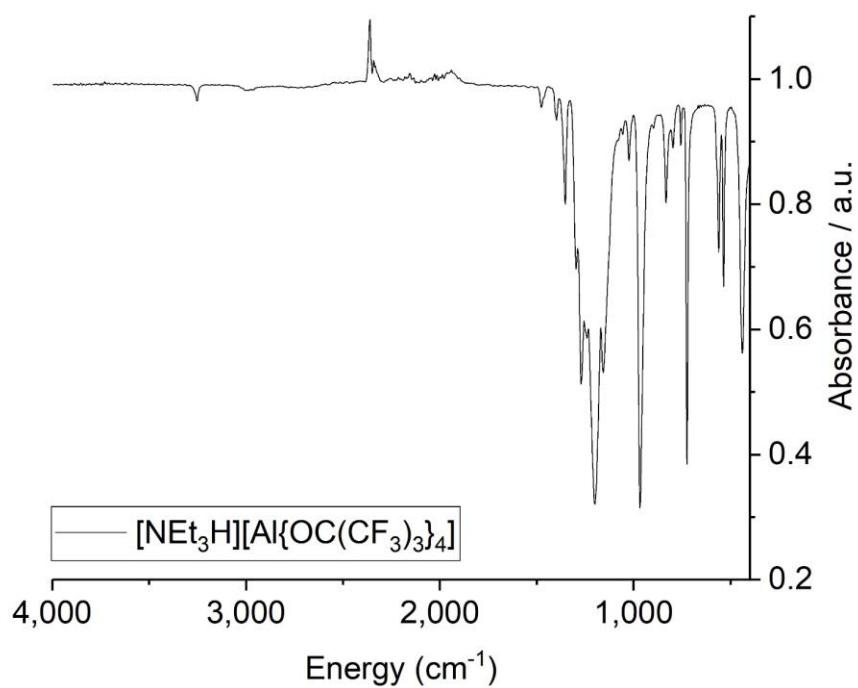


**Figure S5.**  $^{19}\text{F}$  NMR spectrum of  $[\text{NEt}_3\text{H}][\text{Al}\{\text{OC}(\text{CF}_3)_3\}_4]$  in  $\text{CD}_2\text{Cl}_2$ .

#### 4. ATR-IR spectroscopy



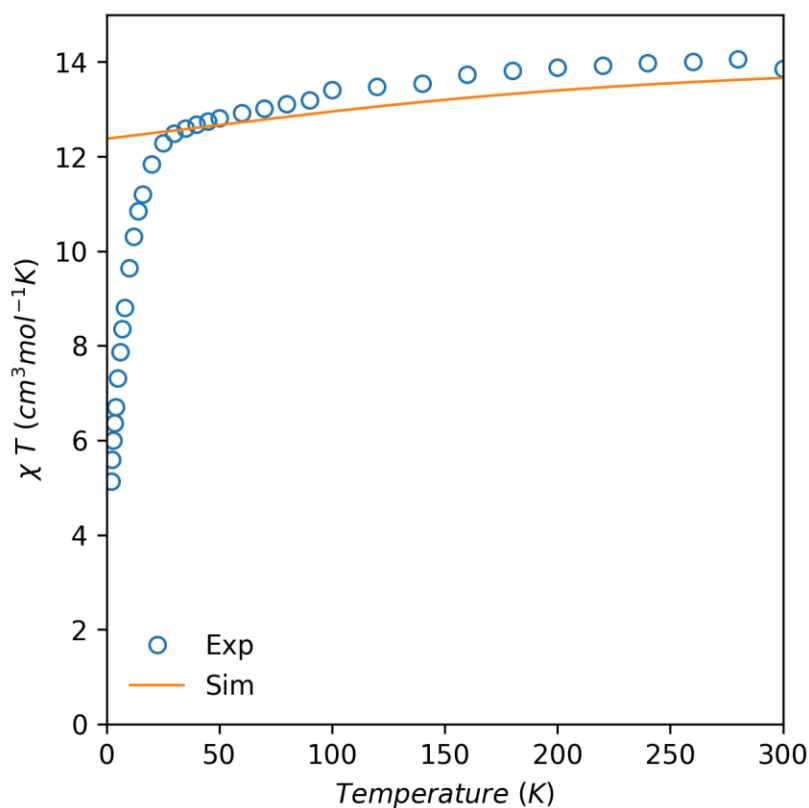
**Figure S6.** ATR-IR spectrum of **1** as a microcrystalline powder.



**Figure S7.** ATR-IR spectrum of [NEt<sub>3</sub>H][Al{OC(CF<sub>3</sub>)<sub>3</sub>}<sub>4</sub>] as a microcrystalline powder.

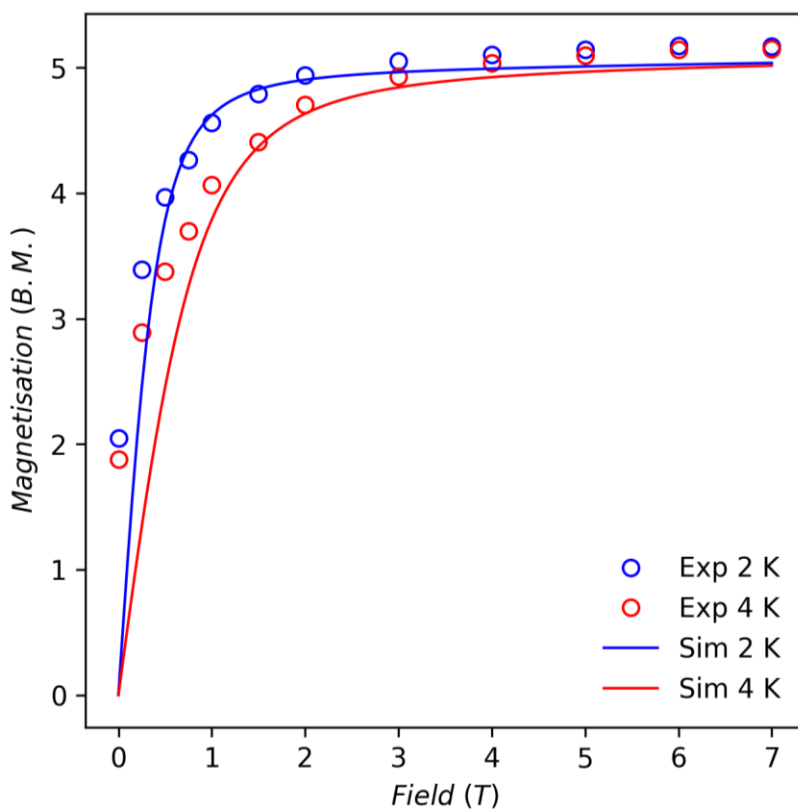
## 5. Magnetic measurements

Magnetic measurements were performed using a Quantum Design MPMS-XL7 superconducting quantum interference device (SQUID) magnetometer. 31.6 mg of a crystalline sample was crushed with a mortar and pestle under an inert atmosphere, and then loaded into a borosilicate glass NMR tube along with 15.4 mg powdered eicosane, which was then evacuated and flame-sealed to a length of *ca.* 5 cm. The eicosane was melted by heating the tube gently with a low-power heat gun in order to immobilize the crystallites. The NMR tube was then mounted in the center of a drinking straw using friction by wrapping it with Kapton tape, and the straw was then fixed to the end of the sample rod. The measurements were corrected for the diamagnetism of the straw, borosilicate tube and eicosane using calibrated blanks, and the intrinsic diamagnetism of the sample using Pascals constant.<sup>7</sup>

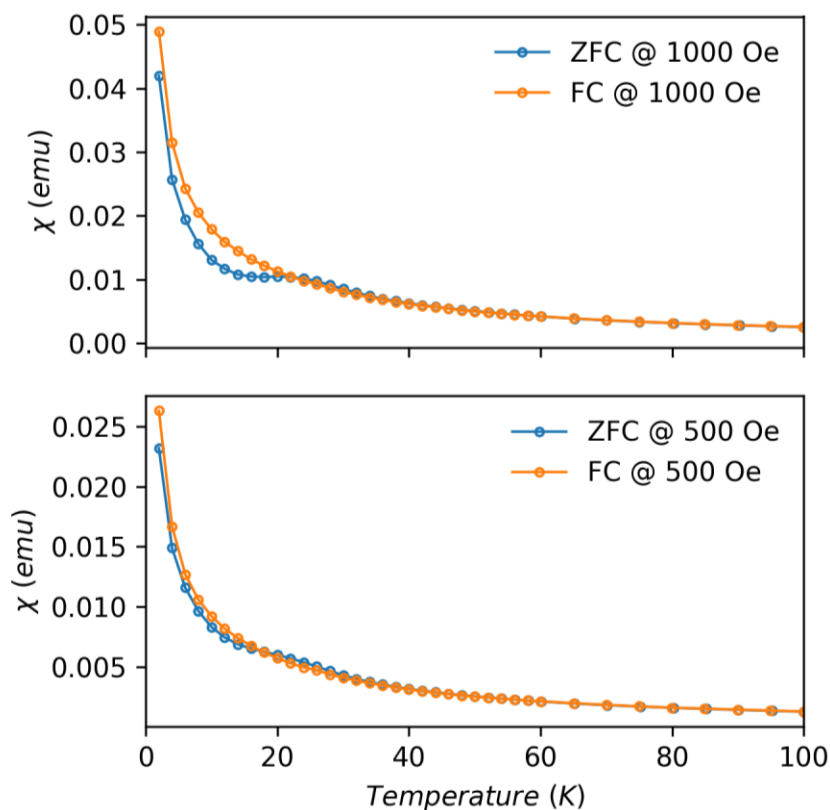


**Figure S8.** Comparison of measured and calculated temperature dependence of the molar magnetic susceptibility  $\chi_M T$  products of **1** measured under a 0.1 T DC field.

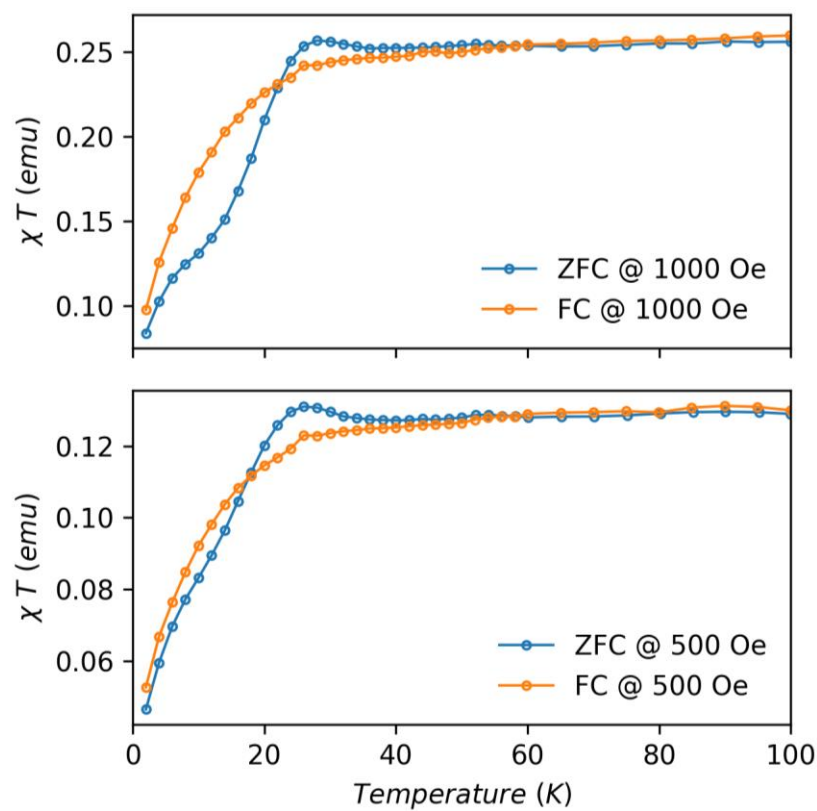




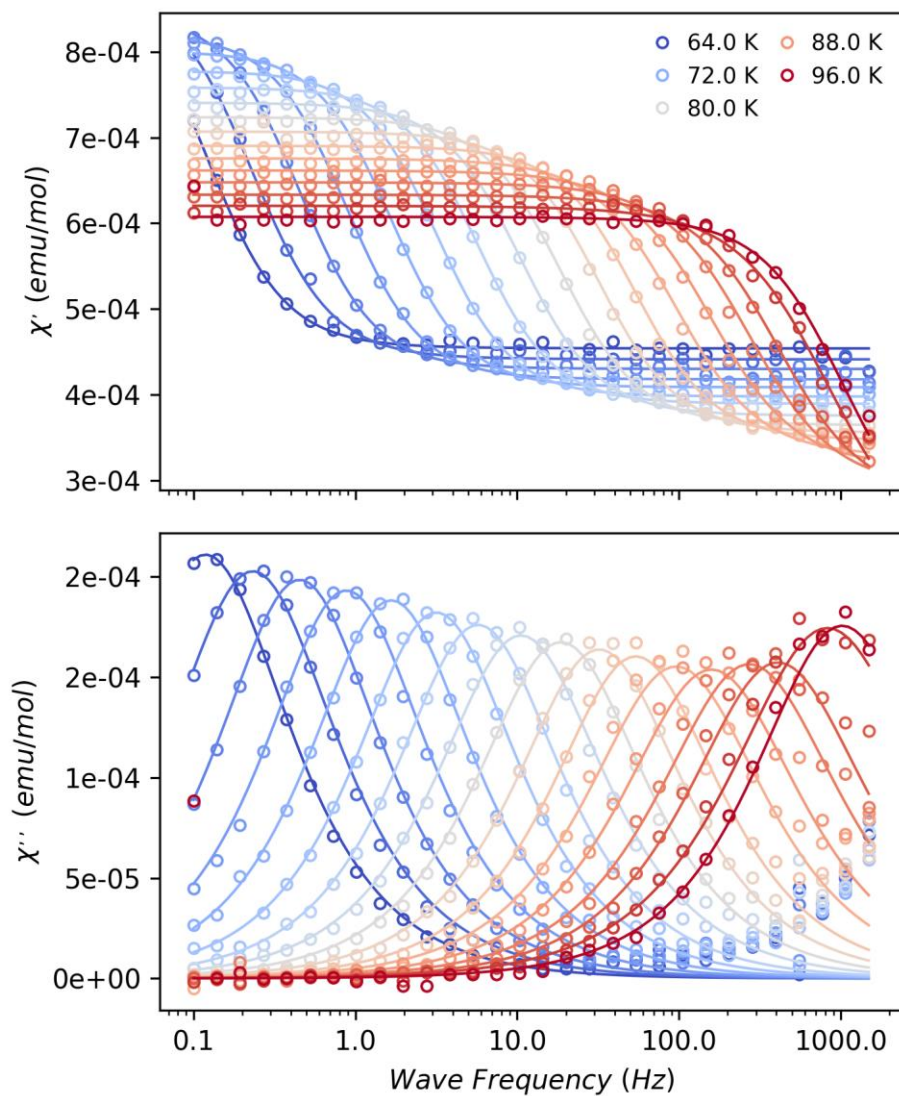
**Figure S9.** Comparison of measured and calculated magnetization curves for **1**.



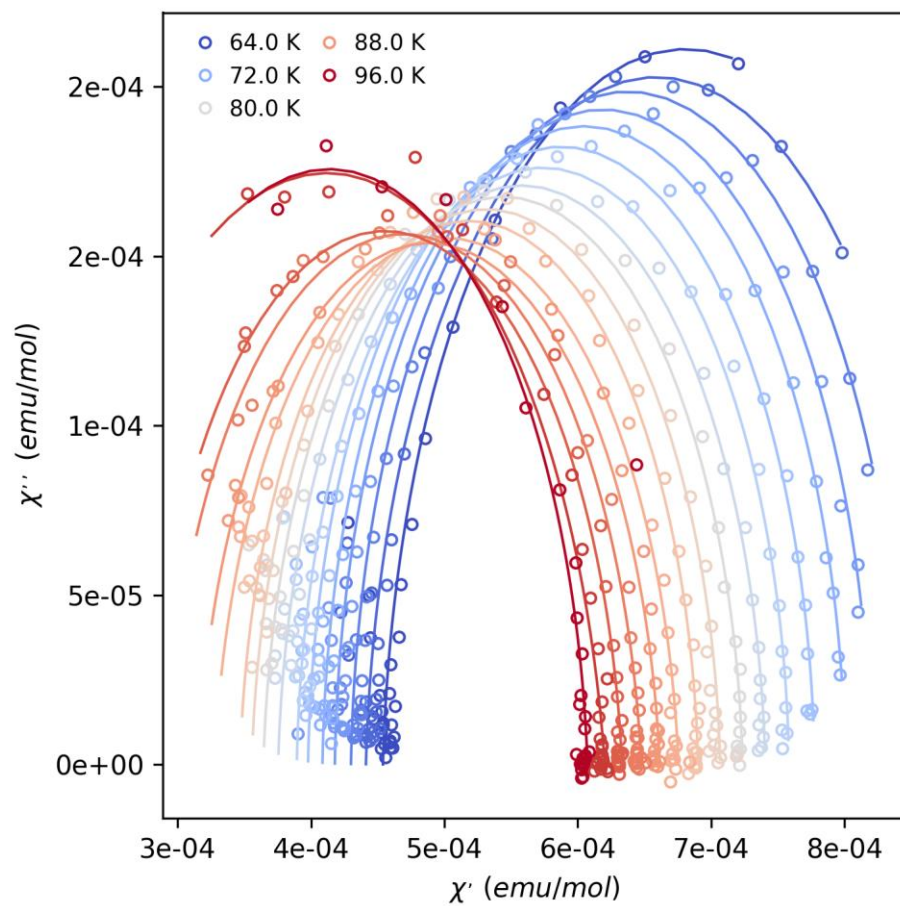
**Figure S10.** Zero-field cooled (ZFC), field cooled (FC) data for **1** under a 0.1 T (top) and 0.05 T (bottom) external field, showing divergence at 25 K.



**Figure S11.** Zero-field cooled (ZFC), field cooled (FC) data for **1** under a 0.1 T (top) and 0.05 T (bottom) external field. The curves overlap at 54 K.



**Figure S12.** In-phase (top) and out-of-phase (bottom) ac susceptibilities in a zero field for **1**. Solid lines are fits to the generalized Debye model, giving  $0.014 \leq \alpha \leq 0.039$ .

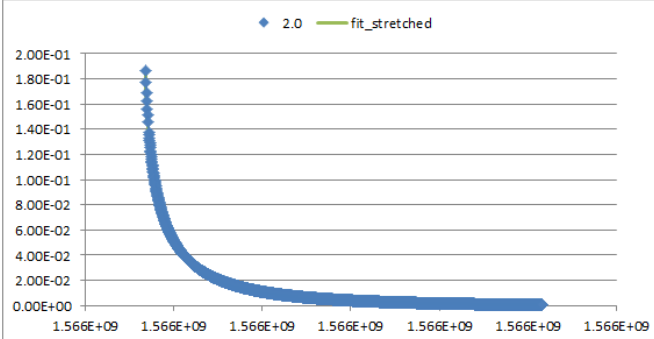
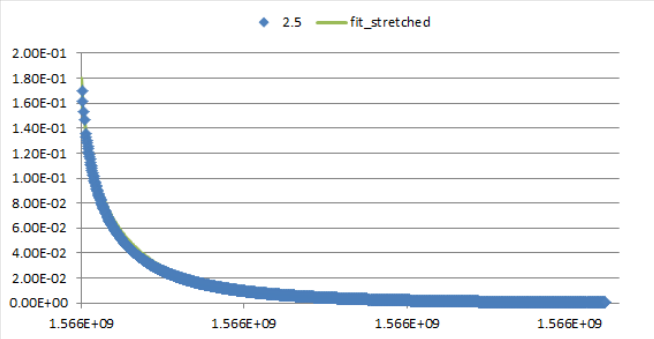
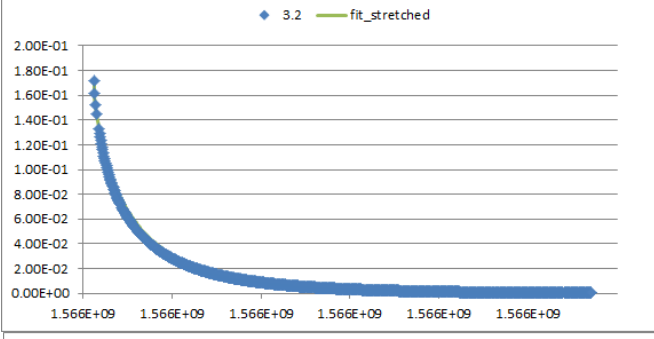
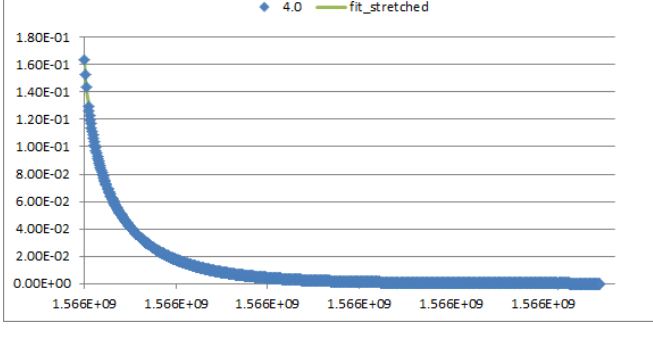


**Figure S13.** Cole-Cole plot for **1**. Solid lines are fits to the generalized Debye model, giving  $0.014 \leq \alpha \leq 0.039$ .

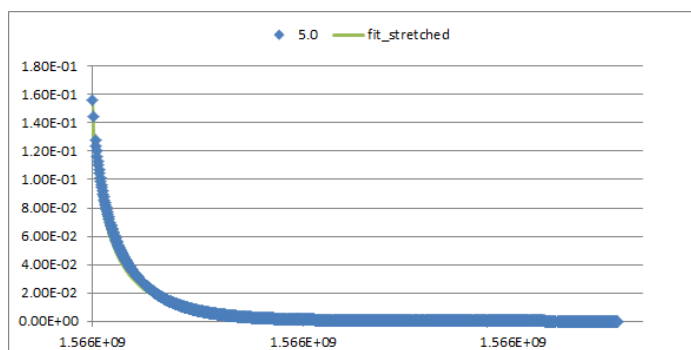
**Table S2.** Best fit parameters to the generalized Debye model.

T	$\tau$	$\tau_{LN}^{err\_upper}$	$\tau_{LN}^{err\_lower}$	$\tau_{Deby}^{err}$	$\chi_S$	$\chi_S^{err}$	$\chi_T$	$\chi_T^{err}$	$\alpha$	$\alpha^{err}$
64.00	1.34E+00	2.03E+00	8.88E-01	1.49E-01	4.01E-06	2.72E-08	8.02E-06	3.21E-07	4.68E-02	0.038
66.00	6.85E-01	1.03E+00	4.56E-01	4.29E-02	3.90E-06	2.90E-08	7.74E-06	1.66E-07	4.54E-02	0.030
68.00	3.52E-01	4.81E-01	2.57E-01	1.64E-02	3.80E-06	3.12E-08	7.46E-06	1.07E-07	2.81E-02	0.027
70.00	1.81E-01	2.43E-01	1.34E-01	7.10E-03	3.69E-06	3.09E-08	7.24E-06	7.44E-08	2.54E-02	0.024
72.00	9.54E-02	1.29E-01	7.05E-02	2.98E-03	3.61E-06	2.68E-08	7.07E-06	4.97E-08	2.62E-02	0.019
74.00	5.02E-02	6.82E-02	3.69E-02	1.56E-03	3.51E-06	2.82E-08	6.87E-06	4.20E-08	2.70E-02	0.019
76.00	2.77E-02	3.85E-02	1.99E-02	1.06E-03	3.44E-06	3.64E-08	6.70E-06	4.53E-08	3.09E-02	0.023
78.00	1.51E-02	2.25E-02	1.01E-02	5.91E-04	3.31E-06	3.93E-08	6.54E-06	4.10E-08	4.47E-02	0.023
80.00	8.51E-03	1.29E-02	5.63E-03	2.91E-04	3.22E-06	3.65E-08	6.39E-06	3.23E-08	4.70E-02	0.020
82.00	4.95E-03	7.43E-03	3.29E-03	1.52E-04	3.14E-06	3.50E-08	6.24E-06	2.63E-08	4.54E-02	0.018
84.00	2.93E-03	4.39E-03	1.96E-03	8.81E-05	3.06E-06	3.70E-08	6.10E-06	2.35E-08	4.48E-02	0.018
86.00	1.65E-03	2.81E-03	9.70E-04	5.68E-05	2.89E-06	4.68E-08	5.97E-06	2.36E-08	7.34E-02	0.019
88.00	9.99E-04	1.72E-03	5.81E-04	2.92E-05	2.78E-06	4.43E-08	5.84E-06	1.80E-08	7.57E-02	0.016
90.00	5.84E-04	1.04E-03	3.29E-04	1.60E-05	2.57E-06	4.78E-08	5.72E-06	1.46E-08	8.34E-02	0.014
92.00	3.85E-04	6.84E-04	2.17E-04	1.44E-05	2.43E-06	7.11E-08	5.60E-06	1.66E-08	8.37E-02	0.018
94.00	1.93E-04	3.81E-04	9.73E-05	8.52E-06	1.80E-06	1.01E-07	5.48E-06	1.27E-08	1.11E-01	0.016
96.00	1.56E-04	2.52E-04	9.61E-05	1.62E-05	1.94E-06	2.48E-07	5.36E-06	2.64E-08	6.19E-02	0.039

**Table S3.** Magnetisation decay curves (points) and stretched exponential fits with the equation  $M(t) = M_2 + (M_1 - M_2)\exp^{-(t/\tau)^\beta}$  (line) at different temperatures.

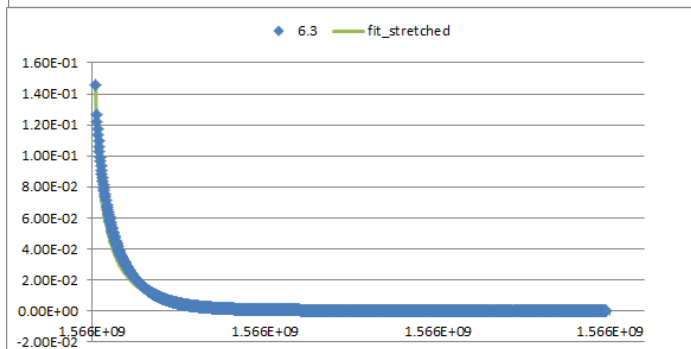
T	Figure	$M_2$ (emu)	$\tau$ (s)	$\beta$
2.0		0.00E+00	1.162E+03	5.973E-01
2.5		0.00E+00	1.004E+03	6.661E-01
3.2		0.00E+00	8.270E+02	7.194E-01
4.0		0.00E+00	6.871E+02	7.382E-01

5.0



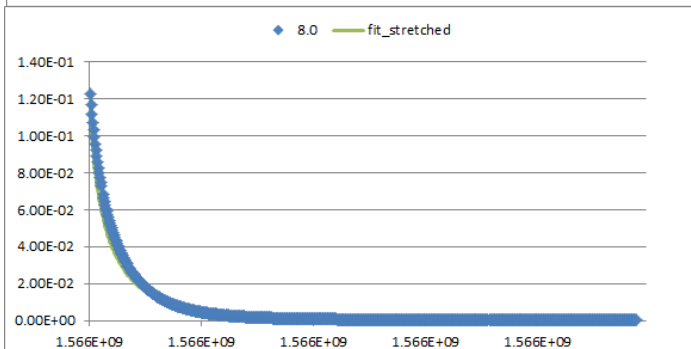
1.81E-05 4.440E+02 6.516E-01

6.3



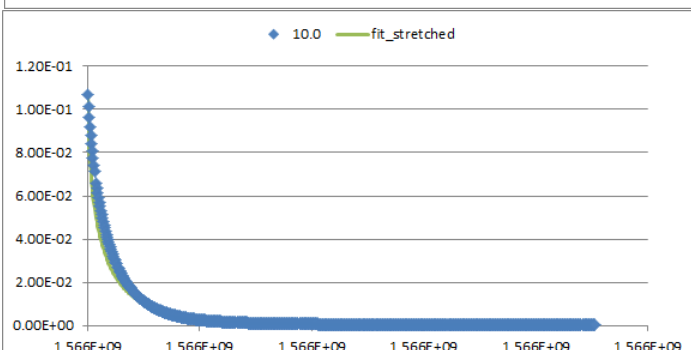
8.10E-05 3.299E+02 6.131E-01

8.0



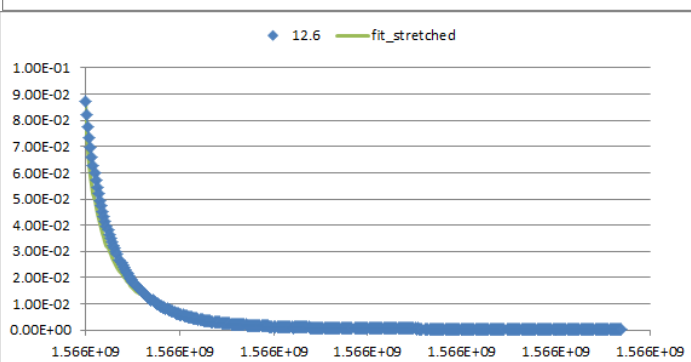
2.05E-04 3.195E+02 6.489E-01

10.0



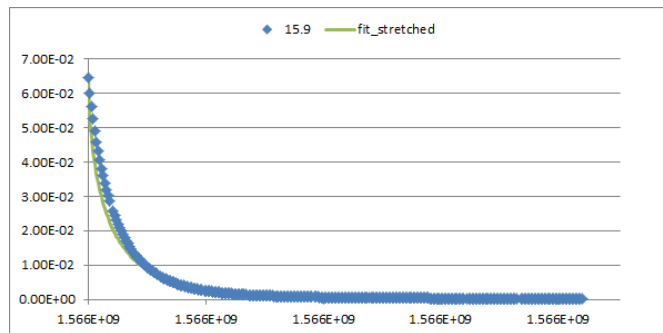
1.99E-04 2.390E+02 6.056E-01

12.6



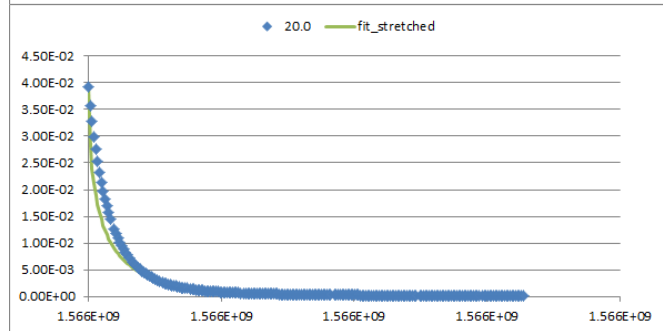
2.70E-04 2.258E+02 6.624E-01

15.9



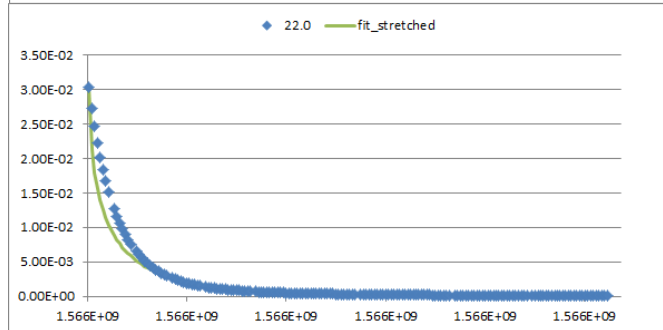
1.96E-04 1.670E+02 6.449E-01

20.0



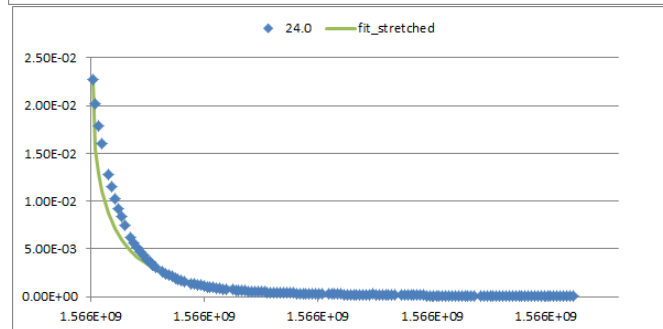
3.84E-05 9.753E+01 5.598E-01

22.0



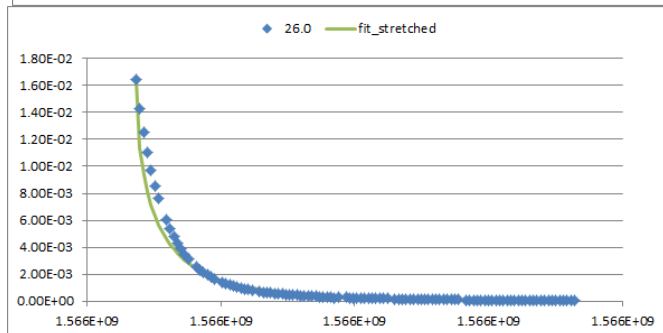
2.41E-05 8.636E+01 5.664E-01

24.0



0.00E+00 7.616E+01 5.655E-01

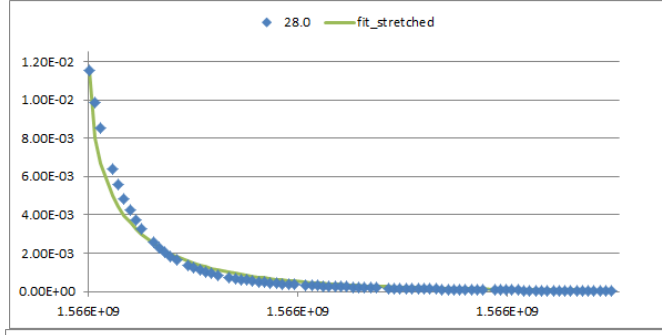
26.0



0.00E+00 7.509E+01 5.996E-01

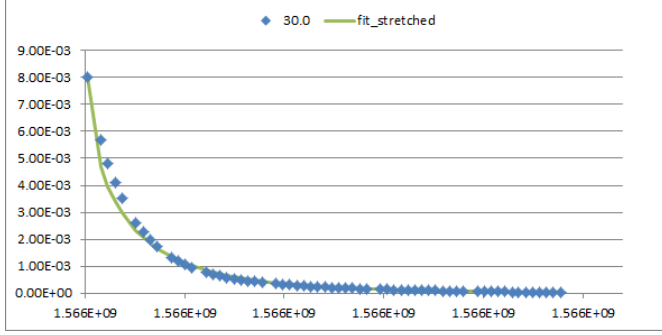


28.0



0.00E+00 7.510E+01 5.996E-01

30.0



0.00E+00 7.079E+01 6.665E-01

In order to determine the range of relaxation times corresponding to *ca.* 68% of the total distribution (*i.e.* the  $1\sigma$  level) around the mean value  $\tau_\mu$  from a stretched exponential function (mirroring our recent work on distributions of relaxation times measured by AC magnetometry<sup>8</sup>), we identify the distribution of relaxation times as defined by Johnston (where  $s = \frac{\tau_\mu}{\tau}$ ):<sup>9</sup>

$$\rho(s, \beta) = \frac{1}{\pi} \int_0^\infty e^{-u^\beta \cos[\pi\beta/2]} \cos[su - u^\beta \sin[\pi\beta/2]] du$$

We then integrate the distribution function in order to determine the exponentially symmetric bounds  $\pm A$  required for any given choice of  $\beta$ :

$$\int_{e^{-A}}^{e^A} \rho(s, \beta) ds = \frac{1}{\sqrt{\pi}} \int_{-\frac{1}{\sqrt{2}}}^{\frac{1}{\sqrt{2}}} e^{-x^2} dx$$

By definition,  $A \rightarrow 0$  for  $\beta \rightarrow 1$  as this defines purely single exponential relaxation, and  $A$  increases with increasing  $\beta$  and approaches  $A \rightarrow \infty$  as  $\beta \rightarrow 0$  when the distribution of relaxation times becomes infinitely broad (Figure

S14). We fit the empirical relationship between  $A$  and  $\beta$  with the function  $A \approx \frac{1.64 \tan[\frac{\pi}{2}(1-\beta)]}{(1-\beta)^{0.141}}$ , that serves to

interpolate the numerical results very well. Hence we define:  $\tau_{\pm} = \tau_{\mu} e^{\pm \frac{1.64 \tan[\frac{\pi}{2}(1-\beta)]}{(1-\beta)^{0.141}}}$ .

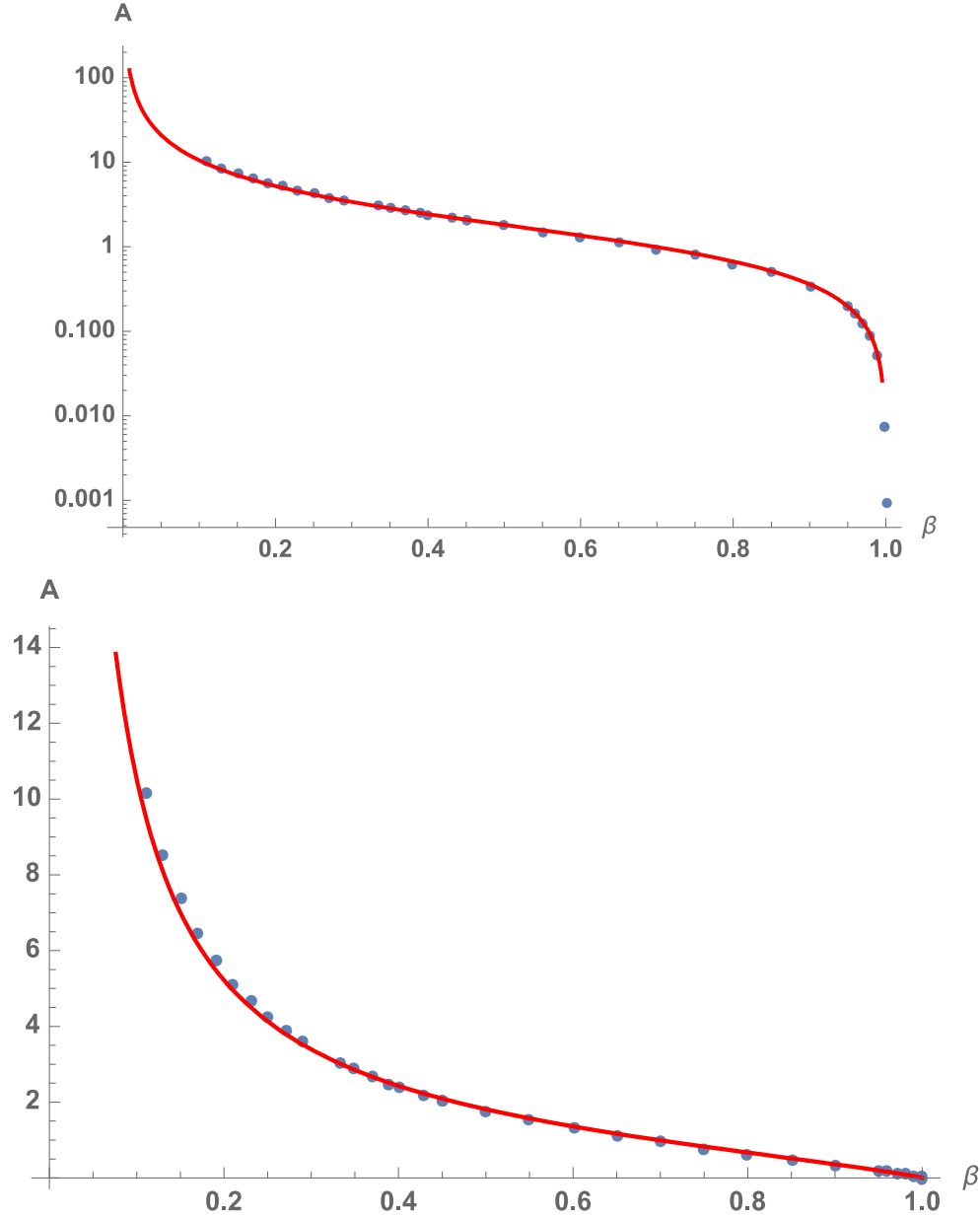


**Figure S14.** Range of  $\pm A$  required to encapsulate  $1\sigma$  populations as a function of  $\beta$  from the distribution underlying the stretched exponential function. Red lines are best fits with  $\approx \frac{1.64 \tan[\frac{\pi}{2}(1-\beta)]}{(1-\beta)^{0.141}}$ .

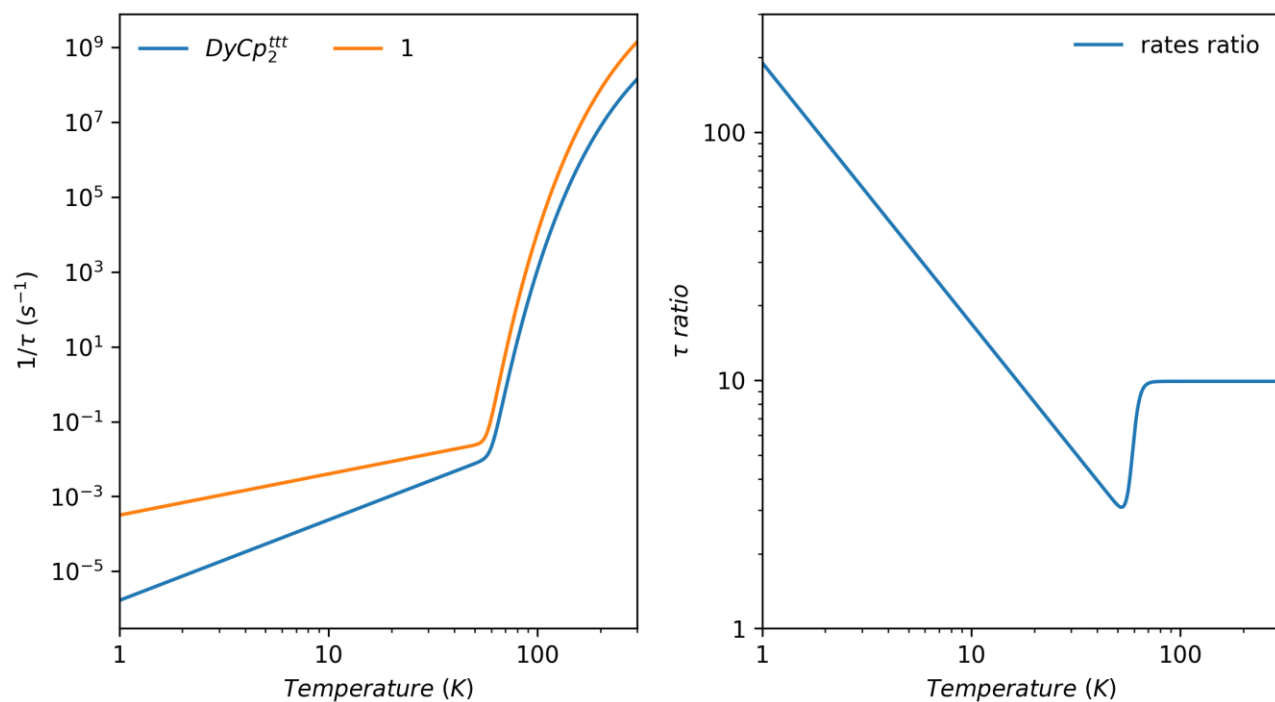


**Figure S15.** (Left) Comparison of relaxation profiles for **1** and  $[\text{Dy}(\text{Cp}^{\text{ttt}})_2][\text{B}(\text{C}_6\text{F}_5)_4]$ . (Right) Ratio between the rates of **1** and those of  $[\text{Dy}(\text{Cp}^{\text{ttt}})_2][\text{B}(\text{C}_6\text{F}_5)_4]$  ( $\tau_1^{-1}/\tau_{[\text{Dy}(\text{Cp}^{\text{ttt}})_2][\text{B}(\text{C}_6\text{F}_5)_4]}^{-1}$ ).

## 6. CASSCF-SO electronic structure and *ab initio* spin dynamics

CASSCF-SO calculations were performed with the program MOLCAS 8.0<sup>10</sup> employing the XRD-determined structure with no optimization and no counterion or solvent molecules. Basis sets from ANO-RCC library<sup>11,12</sup> were employed with VTZP quality for Dy atoms, VDZP quality for the cyclopentadienyl C atoms and VDZ quality for all remaining atoms, employing the second-order DKH transformation. Cholesky decomposition of the two-electron integrals with a threshold of  $10^{-8}$  was performed to save disk space and reduce computational demand. The molecular orbitals (MOs) were optimized in state-averaged CAS(9,7)SCF calculations considering 21, 224 and 490 roots for the sextet, quartet and doublet spin states, respectively. These sets of spin-free states were then used to construct and diagonalize the spin-orbit coupling Hamiltonian in the basis of all sextet, 128 quartet and 130 doublets with the RASSI module. The crystal field decomposition of the ground  $J = 15/2$  multiplet of the  $^6\text{H}$  term was performed with the SINGLE\_ANISO<sup>13</sup> module.

Geometry optimization of the cation in **1** was performed with the Gaussian 09d suite of programs,<sup>14</sup> employing the pure exchange-correlation PBE functional.<sup>15</sup> The Dy atom was substituted by Y to avoid convergence problems associated with the open-shell character of Dy(III) – the isotopic mass of Y was set to 162.5, the atomic weight of Dy. The Y atom was treated with the Stuttgart RSC 1997 ECP,<sup>16</sup> the aromatic carbon atoms of the cyclopentadienyl with cc-pVTZ<sup>17</sup> and the remaining atoms with cc-pVDZ.<sup>18</sup> Empirical dispersion corrections (gd3)<sup>19</sup> were also accounted for. At the optimized geometry, explicit calculation of the Hessian reveals that it is a true local minimum with all frequencies positive and forces zero. The optimized geometry is a good match with the experimental crystal structure of **1**, with a minimized RMSD value of 0.25 Å.<sup>20</sup> In this case we have not calibrated the vibrational frequencies to the IR spectrum of **1**, and rather have opted for a fully *ab initio* calculation in this case.

To determine the spin-phonon coupling of each vibrational mode, we distort the molecule along the normal mode coordinate and perform CASSCF-SO calculations, as described above (except that in this case we use the atomic-compact Cholesky decomposition (acCD) method to generate an auxiliary basis to use the resolution of the identity (RI) approximation),<sup>21</sup> at each point. Assuming the harmonic approximation for each mode, we calculate the thermally averaged displacement at 150 K and displace the molecule up to  $\pm 16\times$ ,  $\pm 10\times$ ,  $\pm 7\times$  the zero-point displacement (ZPD) for modes 1 – 3, respectively,  $\pm 5\times$  ZPD for modes 4 and 5,  $\pm 4\times$  ZPD for modes 6 – 8,  $\pm 3\times$  for modes 9 – 13,  $\pm 2\times$  ZPD for modes 14 – 41, and  $\pm 1.5\times$  ZPD for the remaining modes. We calculate the

electronic structure with CASSCF-SO at 4 evenly spaced points in both positive and negative directions, and then fit the changes in the crystal field parameters (compared to those calculated at the equilibrium geometry) to cubic polynomials. The method as described here differs from that employed in our original work on  $[\text{Dy}(\text{Cp}^{\text{III}})_2][\text{B}(\text{C}_6\text{F}_5)_4]$ ,<sup>22</sup> and so we have repeated the calculations using the revised methodology (we have retained the originally-reported calibration of the vibrational mode energies to the IR and Raman spectra). Hence, we have also calculated the thermally averaged displacement at 150 K and displace the molecule up to  $\pm 14\times$ ,  $\pm 12\times$ ,  $\pm 8\times$ ,  $\pm 7\times$ ,  $\pm 6$  ZPD for modes 1 – 5, respectively,  $\pm 5\times$  ZPD for modes 6 – 8,  $\pm 4\times$  ZPD for mode 9,  $\pm 3\times$  for modes 10 – 13,  $\pm 2\times$  ZPD for modes 14 – 43, and  $\pm 1.5\times$  ZPD for the remaining modes. The states at the equilibrium geometry are very similar to those reported previously (Table S6),<sup>22</sup> and the relaxation rates are now in better agreement with the experiment (Figure S16).

Following our previously described method,<sup>22</sup> we calculate the transition rates from single-phonon processes between each state in the crystal field eigenbasis of the geometry-optimized molecule (here we have applied a magnetic field of 2 Oe along the main magnetic axis to replicate the experimental AC field). However, here we have employed quadruple precision arithmetic throughout, and tested if there is any effect of allowing temperature-dependence in the spin-phonon coupling parameters by altering the vibrational displacement as a function of temperature and determining the appropriate crystal field parameters from the cubic polynomials: we find no difference compared with using a fixed set of spin-phonon coupling matrix elements. Diagonalization of the master matrix gives the relaxation rates, where one is zero corresponding to thermodynamic equilibrium, one is slow corresponding to relaxation over the barrier and the remaining 14 are fast, corresponding to spin motion on either side of the barrier.

We have calculated the strength of the modifications to the crystal field parameters<sup>23</sup> for each vibrational mode, where the parameters below are in Wybourne notation.

$$S = \left[ \frac{1}{3} \sum_k \frac{1}{2k+1} \sum_{q=-k}^k |B_q^k|^2 \right]^{1/2}$$

**Table S4.** Electronic structure of **1** calculated with CASSCF-SO at the solid-state geometry, quantized along the  $g_3$  direction of the ground doublet.

Energy (cm <sup>-1</sup> )	Energy (K)	$g_1$	$g_2$	$g_3$	angle (deg)	Wavefunction	$\langle J_z \rangle$
0.00	0.00	0.00	0.00	19.90	--	98% $ \pm 15/2\rangle$ + 2% $ \pm 11/2\rangle$	$\pm 7.48$
427.42	614.99	0.00	0.00	17.08	4.73	98% $ \pm 13/2\rangle$ + 2% $ \pm 15/2\rangle$	$\pm 6.51$
668.76	962.25	0.00	0.00	14.47	7.55	99% $ \pm 11/2\rangle$ + 1% $ \pm 13/2\rangle$	$\pm 5.51$
834.33	1200.47	0.03	0.03	11.82	2.06	99% $ \pm 9/2\rangle$	$\pm 4.49$
971.87	1398.37	0.55	0.58	9.30	10.63	96% $ \pm 7/2\rangle$ + 3% $ \pm 5/2\rangle$	$\pm 3.46$
1096.91	1578.29	0.05	1.21	6.47	11.71	86% $ \pm 5/2\rangle$ + 8% $ \pm 3/2\rangle$ + 3% $ \pm 7/2\rangle$ + 2% $ \mp 5/2\rangle$ + 2% $ \mp 5/2\rangle$	$\pm 2.30$
1192.88	1716.38	2.99	6.97	8.22	89.20	70% $ \pm 3/2\rangle$ + 14% $ \mp 1/2\rangle$ + 11% $ \pm 1/2\rangle$ + 4% $ \pm 5/2\rangle$	$\pm 1.14$
1285.85	1850.15	0.57	2.22	17.39	89.13	41% $ \pm 1/2\rangle$ + 32% $ \mp 1/2\rangle$ + 21% $ \pm 3/2\rangle$ + 4% $ \pm 5/2\rangle$	$\pm 0.46$

**Table S5.** Electronic structure of **1** calculated with CASSCF-SO at the optimized geometry, quantized along the  $g_3$  direction of the ground doublet.

Energy (cm <sup>-1</sup> )	Energy (K)	$g_1$	$g_2$	$g_3$	angle (deg)	Wavefunction	$\langle J_z \rangle$
0.00	0.00	0.00	0.00	20.00	--	98% $ \pm 15/2\rangle$ + 2% $ \pm 13/2\rangle$	$\pm 7.48$
425.59	612.29	0.00	0.00	17.14	4.76	97% $ \pm 13/2\rangle$ + 2% $ \pm 15/2\rangle$	$\pm 6.51$
654.77	942.02	0.00	0.00	14.56	8.87	99% $ \pm 11/2\rangle$ + 1% $ \pm 13/2\rangle$	$\pm 5.51$
805.76	1159.24	0.01	0.01	11.90	2.91	99% $ \pm 9/2\rangle$	$\pm 4.49$
935.26	1345.56	0.60	0.67	9.37	11.43	95% $ \pm 7/2\rangle$ + 4% $ \pm 5/2\rangle$	$\pm 3.46$
1061.72	1527.50	0.32	0.93	6.52	10.96	86% $ \pm 5/2\rangle$ + 8% $ \pm 3/2\rangle$ + 4% $ \pm 7/2\rangle$	$\pm 2.37$
1165.21	1676.38	3.21	5.72	7.46	90.00	72% $ \mp 3/2\rangle$ + 13% $ \mp 1/2\rangle$ + 9% $ \pm 1/2\rangle$ + 5% $ \mp 5/2\rangle$	$\pm 1.21$
1250.95	1799.74	0.77	3.49	16.52	89.20	51% $ \pm 1/2\rangle$ + 27% $ \mp 1/2\rangle$ + 19% $ \pm 3/2\rangle$ + 3% $ \pm 5/2\rangle$	$\pm 0.54$

**Table S6.** Electronic structure of  $[\text{Dy}(\text{Cp}^{\text{III}})_2][\text{B}(\text{C}_6\text{F}_5)_4]$  calculated with CASSCF-SO at the optimized geometry, quantized along the  $g_3$  direction of the ground doublet.

Energy ( $\text{cm}^{-1}$ )	Energy (K)	$g_1$	$g_2$	$g_3$	angle (deg)	Wavefunction	$\langle J_z \rangle$
0.00	0.00	0.00	0.00	19.99	--	$100\% \pm 15/2\rangle$	$\pm 7.49$
460.98	663.21	0.00	0.00	17.08	1.58	$100\% \pm 13/2\rangle$	$\pm 6.50$
728.38	1047.91	0.00	0.00	14.45	2.85	$99\% \pm 11/2\rangle$	$\pm 5.50$
900.42	1295.44	0.00	0.01	11.79	2.80	$99\% \pm 9/2\rangle$	$\pm 4.48$
1057.68	1521.69	0.06	0.06	9.12	3.65	$98\% \pm 7/2\rangle + 1\% \pm 5/2\rangle$	$\pm 3.49$
1207.60	1737.38	1.05	1.29	6.43	1.94	$97\% \pm 5/2\rangle + 1\% \pm 9/2\rangle + 1\% \pm 7/2\rangle$	$\pm 2.50$
1324.41	1905.42	3.36	3.97	7.37	90.00	$85\% \mp 3/2\rangle + 8\% \pm 1/2\rangle + 5\% \pm 3/2\rangle$	$\pm 1.17$
1407.80	2025.39	0.89	4.48	15.57	89.60	$72\% \pm 1/2\rangle + 18\% \mp 1/2\rangle + 6\% \pm 3/2\rangle + 3\% \mp 3/2\rangle$	$\pm 0.32$

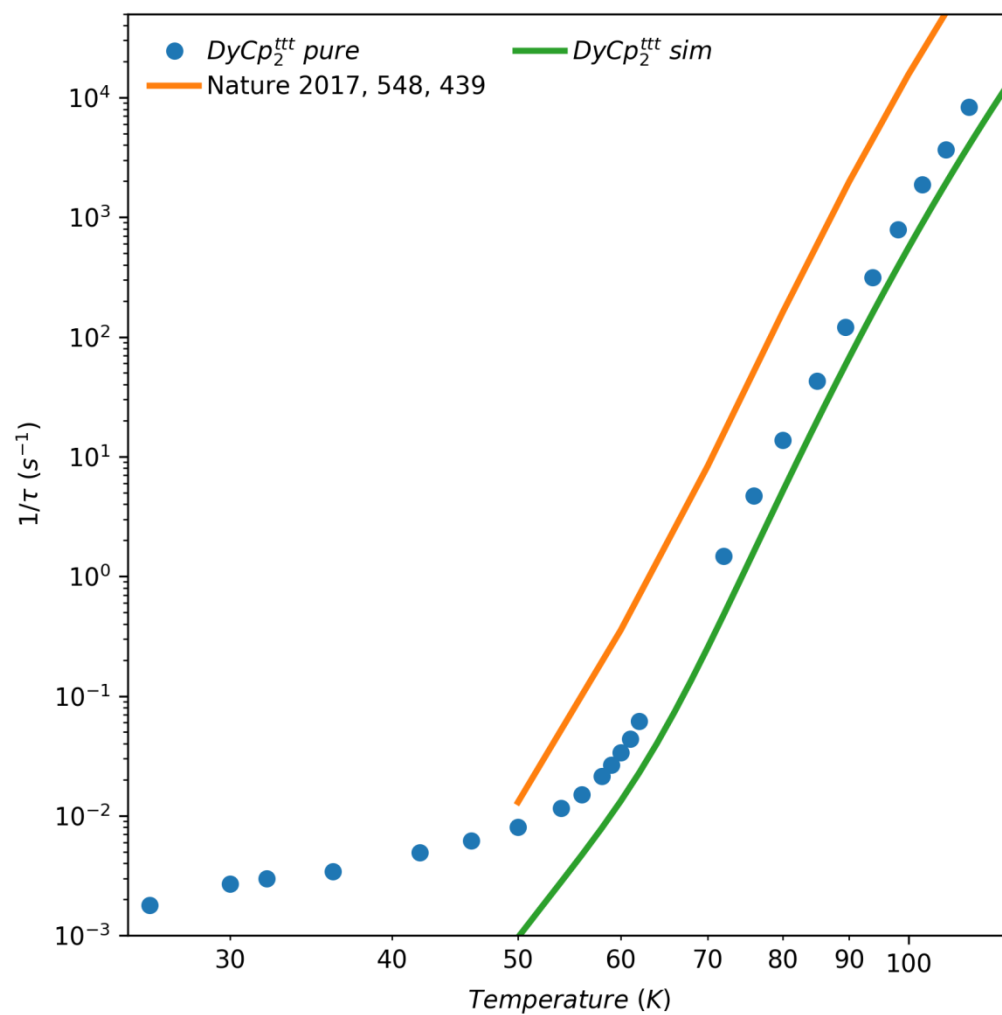


**Figure S16.** Comparison of experimental (points) and *ab initio* calculated (orange: original work,<sup>22</sup> green: this work) magnetic relaxation rates for  $[\text{Dy}(\text{Cp}^{\text{ttt}})_2][\text{B}(\text{C}_6\text{F}_5)_4]$ .



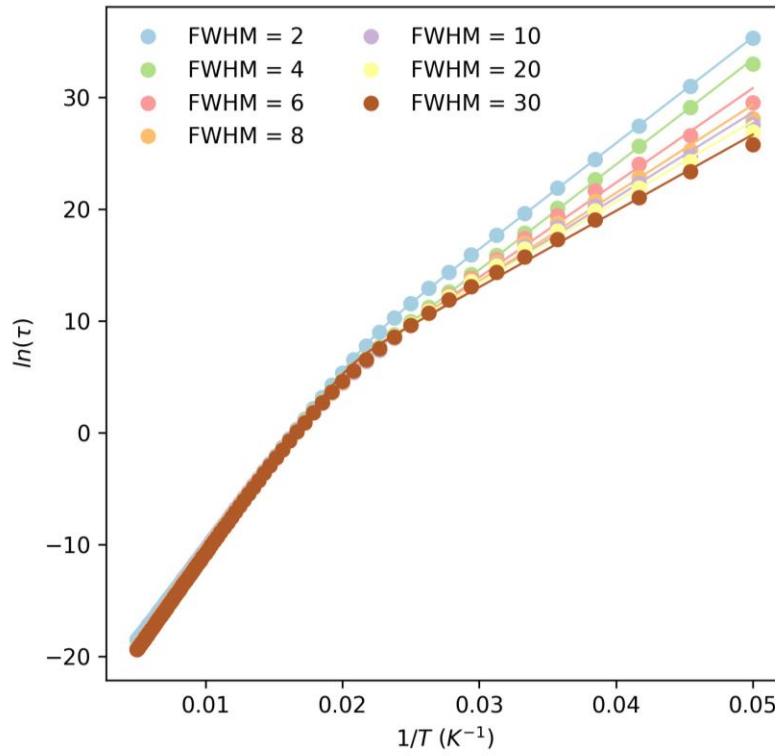


**Figure S17.** Profiles of calculated relaxation times (circles) and their fits (solid lines) at different full width half-maxima, fitted with a combination of two Orbach processes:  $\tau^{-1} = \tau_{0,1}^{-1} e^{\left(-U_1^{eff}/kT\right)} + \tau_{0,2}^{-1} e^{\left(-U_2^{eff}/kT\right)}$ .

**Table S7.** Best fit parameters to the two Orbach processes.

FWHM (cm <sup>-1</sup> )	$\tau_{0,1}$ (s)	$U_1^{eff}$ (K)	$\tau_{0,2}$ (s)	$U_2^{eff}$ (K)
2	2.88E-12	1617	6.23E-06	947
4	1.07E-12	1693	1.15E-06	941
6	1.20E-12	1677	1.05E-05	845
8	1.29E-12	1667	4.14E-05	788
10	1.33E-12	1663	7.78E-05	762
20	1.21E-12	1658	2.41E-04	724
30	1.15E-12	1660	5.80E-04	682

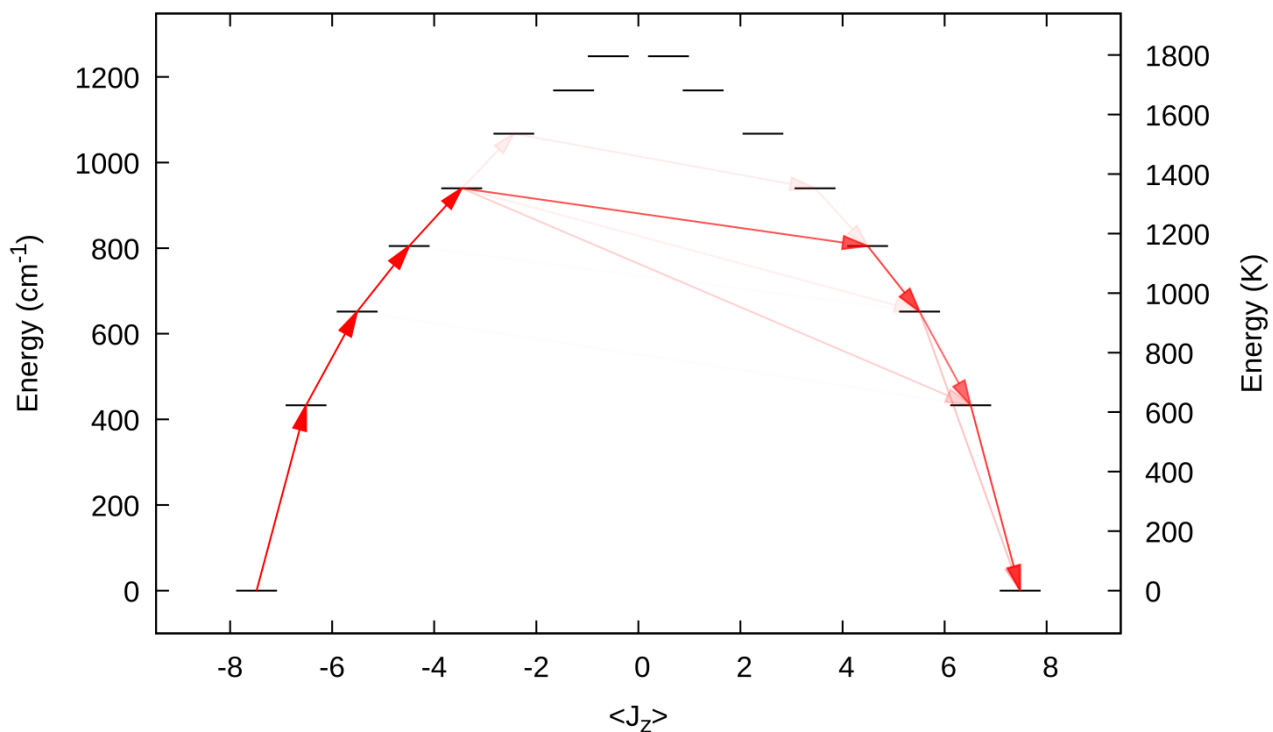


**Figure S18.** Energy barrier to magnetic relaxation for **1**, calculated at 20 K and using  $\text{FWHM} = 6 \text{ cm}^{-1}$ . Electronic states from CASSCF-SO calculations, decomposed in the  $J = 15/2$  basis. The opacity of the arrows are proportional to the single-phonon transition probability normalized from each departing state and commencing with unit population in  $|-15/2\rangle$ ; only relaxation pathways towards  $|+15/2\rangle$  are shown.  $\langle J_z \rangle$  is the expectation value of the  $J_z$  operator along the quantization axis.

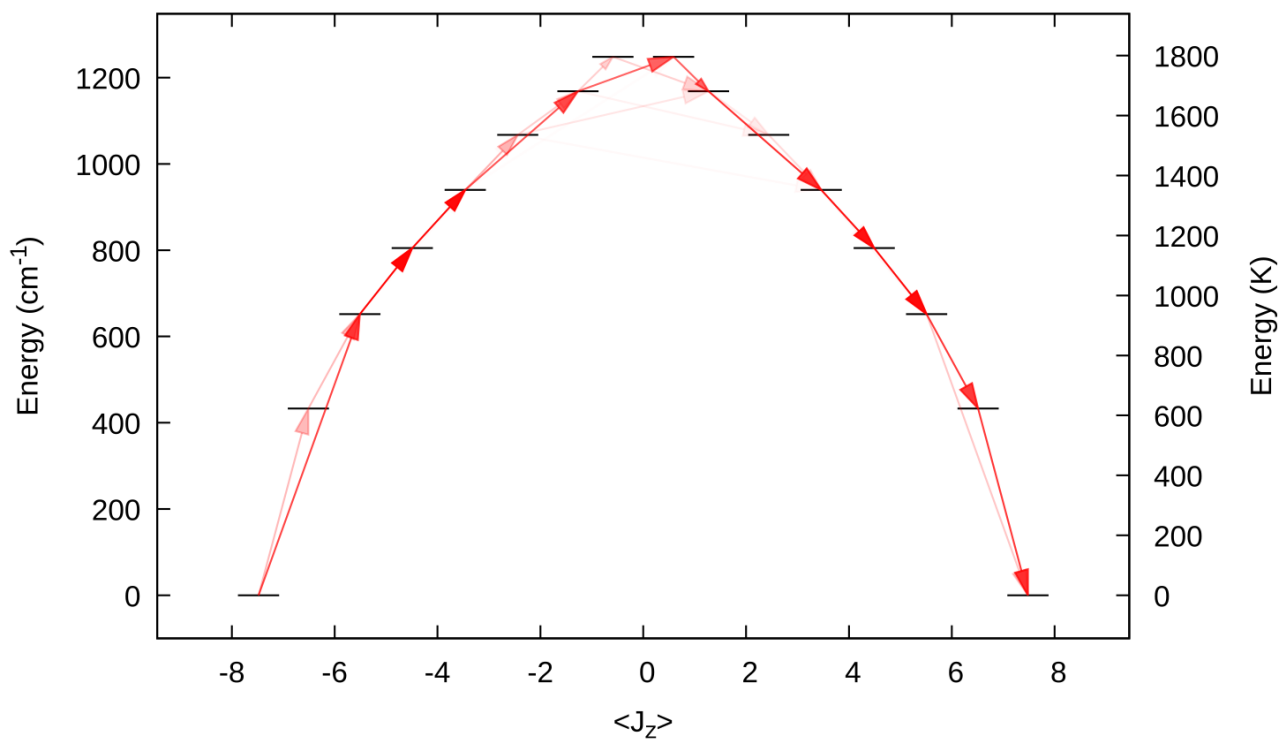


**Figure S19.** Energy barrier to magnetic relaxation for **1**, calculated at 300 K and using FWHM = 6 cm<sup>-1</sup>. Electronic states from CASSCF-SO calculations, decomposed in the  $J = 15/2$  basis. The opacity of the arrows are proportional to the single-phonon transition probability normalized from each departing state and commencing with unit population in  $|-15/2\rangle$ ; only relaxation pathways towards  $|+15/2\rangle$  are shown.  $\langle J_z \rangle$  is the expectation value of the  $J_z$  operator along the quantization axis.

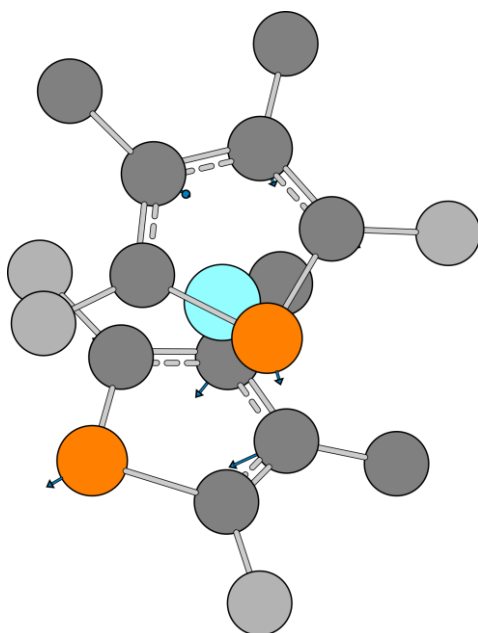


**Figure S20.** Schematic representation of the mode with the largest contribution to the  $|15/2\rangle \rightarrow |13/2\rangle$  in **1**. Blue, orange and grey colors stand for dysprosium, phosphorus and carbon atoms. Light grey indicates the *tert*-butyl (not shown for clarity) substituted carbon atoms.

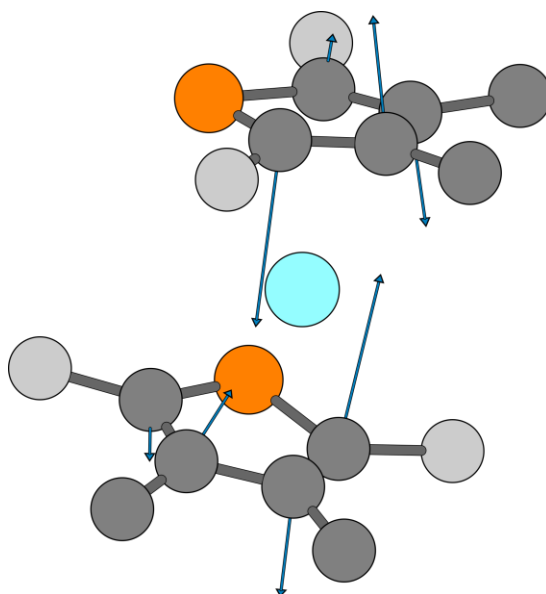


**Figure S21.** Schematic representation of mode causing the first step in magnetic relaxation in **1**. Blue, orange and grey colors stand for dysprosium, phosphorus, and carbon atoms. Light grey indicates the *tert*-butyl (not shown for clarity) substituted carbon atoms.

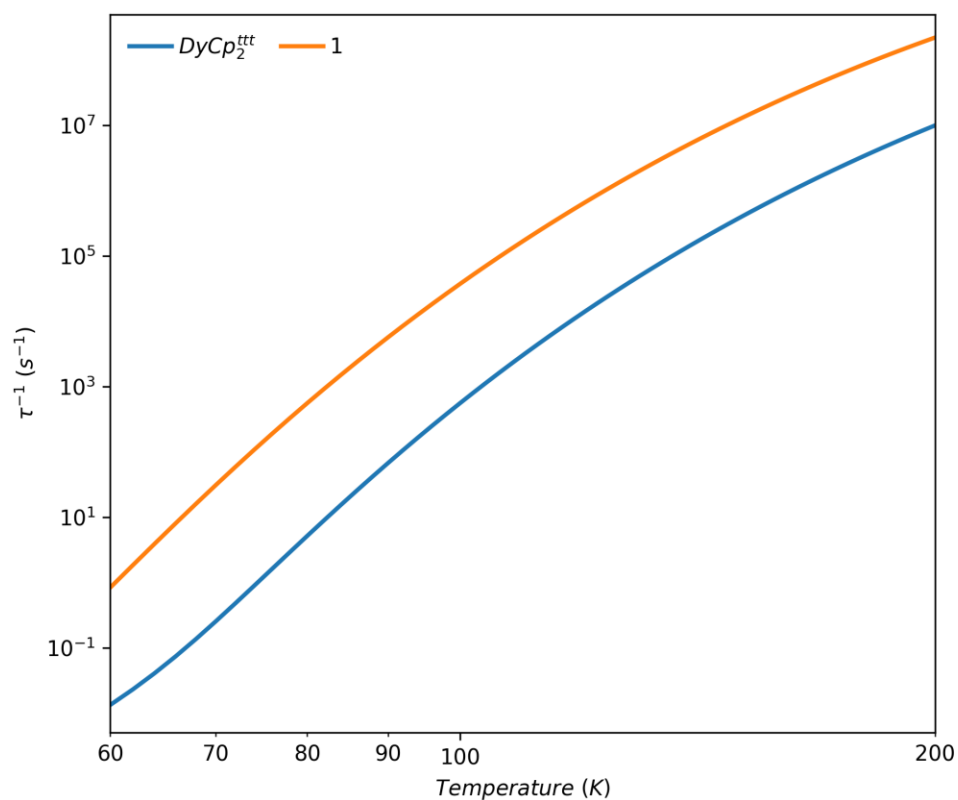


**Figure S22.** Comparison of calculated rates (FWHM = 6 cm<sup>-1</sup>) for [Dy(Cp<sup>ttt</sup>)<sub>2</sub>][B(C<sub>6</sub>F<sub>5</sub>)<sub>4</sub>] and **1**.

**Table S8.** Comparison of escape rates (s<sup>-1</sup>) of the |±15/2⟩ state in [Dy(Cp<sup>ttt</sup>)<sub>2</sub>][B(C<sub>6</sub>F<sub>5</sub>)<sub>4</sub>] and **1**, calculated with FWHM = 6 cm<sup>-1</sup>.

Temperature (K)	[Dy(Cp <sup>ttt</sup> ) <sub>2</sub> ][B(C <sub>6</sub> F <sub>5</sub> ) <sub>4</sub> ] (s <sup>-1</sup> )	<b>1</b> (s <sup>-1</sup> )
50	3.19E+06	1.16E+05
100	2.79E+09	9.11E+07
150	2.79E+10	1.24E+09
300	3.37E+11	2.32E+10

**Table S9.** Comparison of transition rates ( $\text{s}^{-1}$ ) between pairs of electronic states in  $[\text{Dy}(\text{Cp}^{\text{ttt}})_2][\text{B}(\text{C}_6\text{F}_5)_4]$  and **1**, calculated with FWHM =  $6\text{ cm}^{-1}$ .

Temperature (K)	Transition	$[\text{Dy}(\text{Cp}^{\text{ttt}})_2][\text{B}(\text{C}_6\text{F}_5)_4]$ ( $\text{s}^{-1}$ )	<b>1</b> ( $\text{s}^{-1}$ )
50	$ \pm 15/2\rangle$ to $ \pm 13/2\rangle$	$3.19\text{E}+06$	$1.13\text{E}+05$
	$ \pm 15/2\rangle$ to $ \pm 11/2\rangle$	$1.29\text{E}+03$	$2.85\text{E}+03$
100	$ \pm 15/2\rangle$ to $ \pm 13/2\rangle$	$2.74\text{E}+09$	$5.73\text{E}+07$
	$ \pm 15/2\rangle$ to $ \pm 11/2\rangle$	$4.33\text{E}+07$	$3.38\text{E}+07$
150	$ \pm 15/2\rangle$ to $ \pm 13/2\rangle$	$2.65\text{E}+10$	$4.67\text{E}+08$
	$ \pm 15/2\rangle$ to $ \pm 11/2\rangle$	$1.40\text{E}+09$	$7.73\text{E}+08$
300	$ \pm 15/2\rangle$ to $ \pm 13/2\rangle$	$2.90\text{E}+11$	$4.43\text{E}+09$
	$ \pm 15/2\rangle$ to $ \pm 11/2\rangle$	$4.73\text{E}+10$	$1.87\text{E}+10$

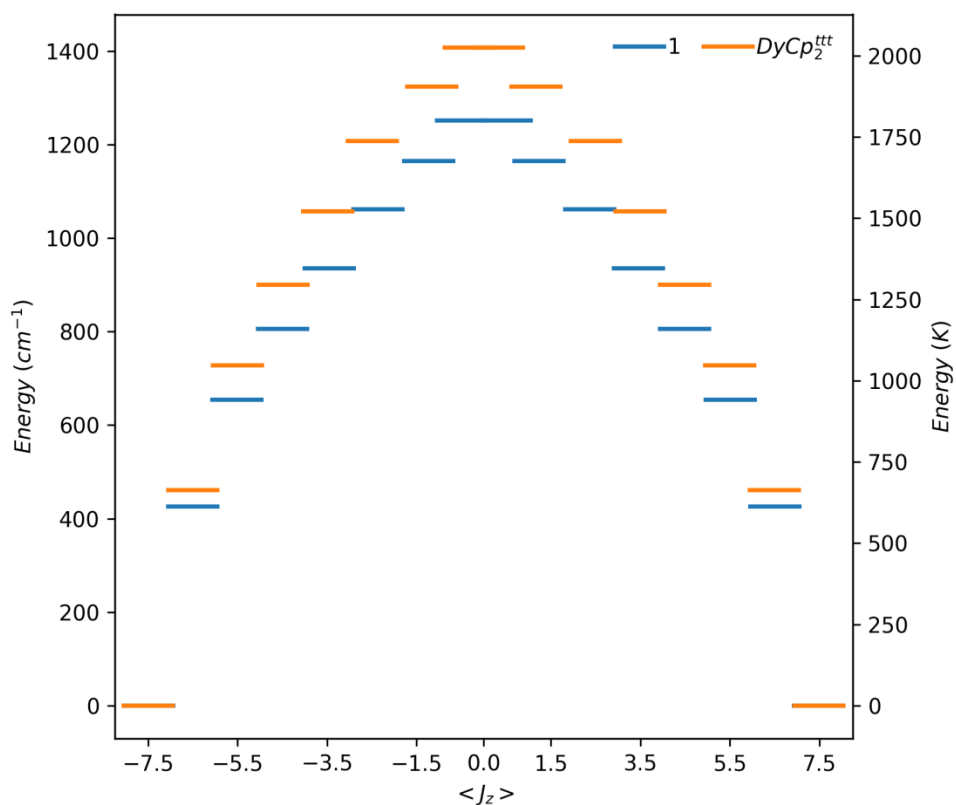


**Figure S23.** Comparison of the electronic structures at the optimized geometries of **1** and  $[\text{Dy}(\text{Cp}^{\text{ttt}})_2][\text{B}(\text{C}_6\text{F}_5)_4]$ .

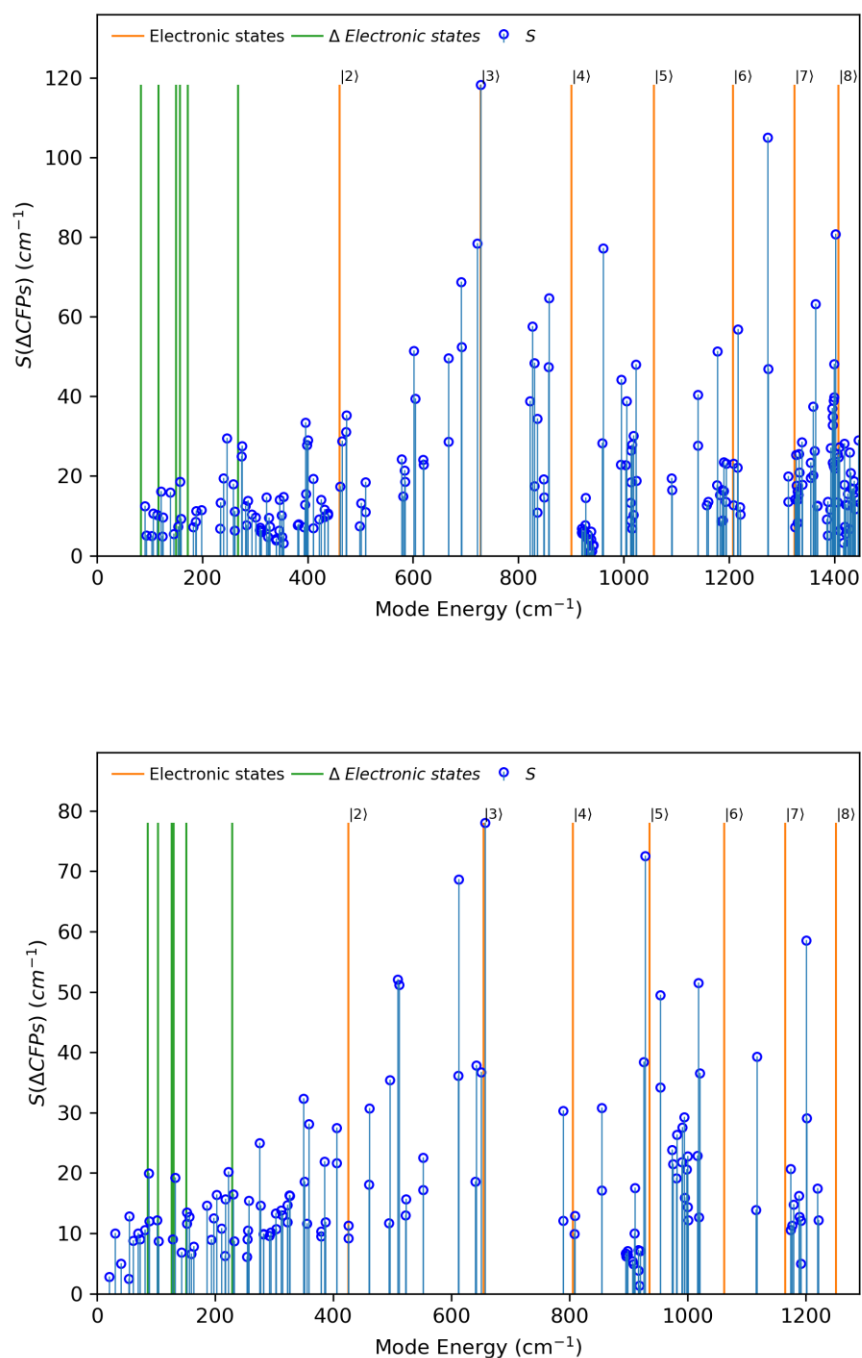


**Figure S24.** Strength of the crystal field distortions induced by each vibrational mode for  $[\text{Dy}(\text{Cp}^{\text{III}})_2][\text{B}(\text{C}_6\text{F}_5)_4]$  (top) and **1** (bottom). Vibrational modes distorted to the zero-point displacement. CASSCF-SO-calculated electronic state energies and their differences are indicated in orange and green, respectively, based on optimized geometries. Electronic states are labelled in increasing order of energy.

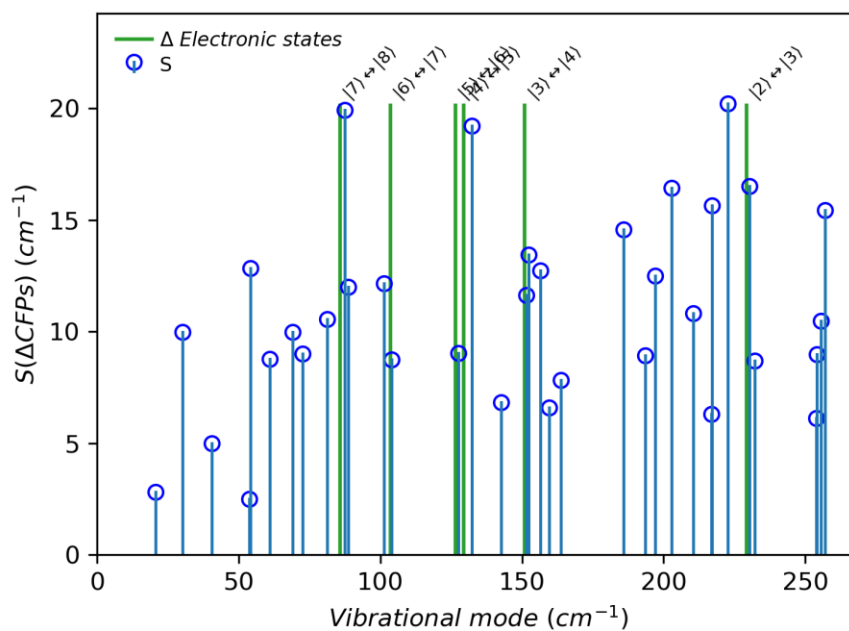
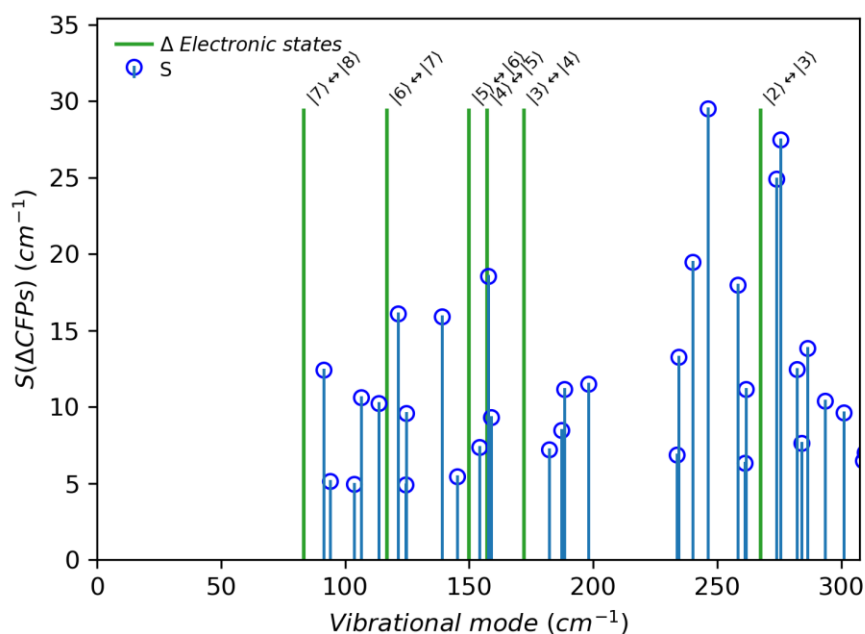


**Figure S25.** Strength of the crystal field distortions induced by each vibrational mode for  $[\text{Dy}(\text{Cp}^{\text{III}})_2][\text{B}(\text{C}_6\text{F}_5)_4]$  (top) and **1** (bottom), in the lower vibrational energy range. Vibrational modes distorted to the zero-point displacement. CASSCF-SO-calculated electronic state energies and their differences are indicated in orange and green, respectively, based on optimized geometries. Electronic states are labelled in increasing order of energy.



**Table S10.** Comparison of transition rates ( $\text{s}^{-1}$ ) between pairs of electronic states in  $[\text{Dy}(\text{Cp}^{\text{III}})_2][\text{B}(\text{C}_6\text{F}_5)_4]$  and **1**, calculated with FWHM =  $6 \text{ cm}^{-1}$ .

Temperature (K)	Transition	$[\text{Dy}(\text{Cp}^{\text{III}})_2][\text{B}(\text{C}_6\text{F}_5)_4]$ ( $\text{s}^{-1}$ )	<b>1</b> ( $\text{s}^{-1}$ )
50	$ \pm 13/2\rangle$ to $ \pm 11/2\rangle$	9.02E+07	1.88E+09
	$ \pm 11/2\rangle$ to $ \pm 9/2\rangle$	1.24E+08	1.44E+10
	$ \pm 9/2\rangle$ to $ \pm 7/2\rangle$	1.03E+08	2.22E+10
100	$ \pm 13/2\rangle$ to $ \pm 11/2\rangle$	3.67E+09	4.66E+10
	$ \pm 11/2\rangle$ to $ \pm 9/2\rangle$	1.73E+09	1.51E+11
	$ \pm 9/2\rangle$ to $ \pm 7/2\rangle$	1.23E+09	1.87E+11
150	$ \pm 13/2\rangle$ to $ \pm 11/2\rangle$	1.36E+10	1.50E+11
	$ \pm 11/2\rangle$ to $ \pm 9/2\rangle$	4.73E+09	3.86E+11
	$ \pm 9/2\rangle$ to $ \pm 7/2\rangle$	3.24E+09	4.49E+11
300	$ \pm 13/2\rangle$ to $ \pm 11/2\rangle$	6.58E+10	6.42E+11
	$ \pm 11/2\rangle$ to $ \pm 9/2\rangle$	1.74E+10	1.33E+12
	$ \pm 9/2\rangle$ to $ \pm 7/2\rangle$	1.16E+10	1.46E+12

---

## 7. References

1. *CrysAlis Pro*, Agilent Technologies: Yarnton, England, **2017**.
2. Sheldrick, G. M. Crystal structure refinement with SHELXL. *Acta Crystallogr. Sect. C* **2015**, *71*, 3–8.
3. Sheldrick, G. M. A short history of SHELX. *Acta Crystallogr. Sect. A* **2008**, *64*, 112–122.
4. Dolomanov, O. V.; Bourhis, L. J.; Gildea, R. J.; Howard, J. A. K.; Puschmann, H. OLEX2: a complete structure solution, refinement and analysis program.. *J. Appl. Crystallogr.* **2009**, *42*, 339–341.
5. Farrugia, L. J. WinGX and ORTEP for Windows: an update. *J. Appl. Crystallogr.* **2012**, *45*, 849–854.
6. *POV-Ray*, Persistence of Vision Raytracer Pty. Ltd.: Williamstown, Australia, **2013**.
7. Bain, G. A.; Berry, J. F. Diamagnetic Corrections and Pascal's Constants. *J. Chem. Ed.* **2008**, *85*, 532.
8. Reta, D.; Chilton, N. F. Uncertainty estimates for magnetic relaxation times and magnetic relaxation parameters. *Phys. Chem. Chem. Phys.* **2019**, *21*, 23567–23575.
9. Johnston, D. C. Stretched exponential relaxation arising from a continuous sum of exponential decays. *Phys. Rev. B* **2006**, *74*, 184430.
10. Aquilante, F.; Autschbach, J.; Carlson, R. K.; Chibotaru, L. F.; Delcey, M. G.; De Vico, L.; Fdez. Galván, I.; Ferré, N.; Frutos, L. M.; Gagliardi, L.; Garavelli, M.; Giussani, A.; Hoyer, C. E.; Manni, G. L.; Lischka, H.; Ma, D.; Malmqvist, P.-Å.; Müller, T.; Nenov, A.; Olivucci, M.; Pedersen, T. B.; Peng, D.; Plasser, F.; Pritchard, B.; Reiher, M.; Rivalta, I.; Schapiro, I.; Segarra-Martí, J.; Stenrup, M.; Truhlar, D. G.; Ungur, L.; Valentini, A.; Vancoillie, S.; Veryazov, V.; Vysotskiy, V. P.; Weingart, O.; Zapata, F.; Lindh, R. MOLCAS 8: New capabilities for multiconfigurational quantum chemical calculations across the periodic table. *J. Comput. Chem.* **2015**, *37*, 506–541.
11. Roos, B. O.; Lindh, R.; Malmqvist, P.-Å.; Veryazov, V.; Widmark, P.-O. New Relativistic ANO Basis Sets for Transition Metal Atoms. *J. Phys. Chem. A* **2005**, *109*, 6575–6579.
12. Roos, B. O.; Lindh, R.; Malmqvist, P.-Å.; Veryazov, V.; Widmark, P.-O. Main Group Atoms and Dimers Studied with a New Relativistic ANO Basis Set. *J. Phys. Chem. A* **2004**, *108*, 2851–2858.
13. L. Ungur, L.; Chibotaru, L. F. Ab Initio Crystal Field for Lanthanides. *Chem. Eur. J.* **2017**, *23*, 3708–3718.

- 
14. Gaussian 09, Revision D.01, Frisch, M. J.; Trucks, G. W.; Schlegel, H. B.; Scuseria, G. E.; Robb, M. A.; Cheeseman, J. R.; Scalmani, G.; Barone, V.; Petersson, G. A.; Nakatsuji, H.; Li, X.; Caricato, M.; Marenich, A.; Bloino, J.; Janesko, B. G.; Gomperts, R.; Mennucci, B.; Hratchian, H. P.; Ortiz, J. V.; Izmaylov, A. F.; Sonnenberg, J. L.; Williams-Young, D.; Ding, F.; Lipparini, F.; Egidi, F.; Goings, J.; Peng, B.; Petrone, A.; Henderson, T.; Ranasinghe, D.; Zakrzewski, V. G.; Gao, J.; Rega, N.; Zheng, G.; Liang, W.; Hada, M.; Ehara, M.; Toyota, K.; Fukuda, R.; Hasegawa, J.; Ishida, M.; Nakajima, T.; Honda, Y.; Kitao, O.; Nakai, H.; Vreven, T.; Throssell, K.; Montgomery, Jr., J. A.; Peralta, J. E. Ogliaro, F.; Bearpark, M.; Heyd, J. J.; Brothers, E.; Kudin, K. N.; Staroverov, V. N.; Keith, T.; Kobayashi, R.; Normand, J.; Raghavachari, K.; Rendell, A.; Burant, J. C.; Iyengar, S. S.; Tomasi, J.; Cossi, M.; Millam, J. M.; Klene, M.; Adamo, C.; Cammi, R.; Ochterski, J. W.; Martin, R. L.; Morokuma, K.; Farkas, O.; Foresman, J. B.; Fox, D. J. Gaussian, Inc., Wallingford CT, USA, **2016**.
15. (a) Perdew, J. P.; Burke, K.; Ernzerhof, M. Generalized Gradient Approximation Made Simple. *Phys. Rev. Lett.* **1996**, *77*, 3865; (b) Perdew, J. P.; Burke, K.; Ernzerhof, M. Generalized Gradient Approximation Made Simple [Phys. Rev. Lett. 77, 3865 (1996)]. *Phys. Rev. Lett.* **1997**, *78*, 1396.
16. (a) Bergner, A.; Dolg, M.; Küchle, W.; Stoll, H.; Preuß, H. *Ab initio* energy-adjusted pseudopotentials for elements of groups 13–17. *Mol. Phys.* **1993**, *80*, 1431–1441; (b) Kaupp, M.; Schleyer, P. v. R.; Stoll, H.; Preuß, H. Pseudopotential approaches to Ca, Sr, and Ba hydrides. Why are some alkaline earth MX<sub>2</sub> compounds bent? *J. Chem. Phys.* **1991**, *94*, 1360; (c) Dolg, M.; Stoll, H.; Preuß, H.; Pitzer, R. M. Relativistic and correlation effects for element 105 (hahnium, Ha): a comparative study of M and MO (M = Nb, Ta, Ha) using energy-adjusted *ab initio* pseudopotentials. *J. Phys. Chem.* **1993**, *97*, 5852–5859.
17. Woon, D. E.; Dunning, T. H. Gaussian basis sets for use in correlated molecular calculations. IV. Calculation of static electrical response properties. *J. Chem. Phys.* **1994**, *100*, 2975.
18. Woon, D. E.; Dunning, T. H. Gaussian basis sets for use in correlated molecular calculations. III. The atoms aluminum through argon. *J. Chem. Phys.* **1993**, *98*, 1358.
19. Grimme, S. Density functional theory with London dispersion corrections. *Wiley Interdiscip. Rev. Comput. Mol. Sci.* **2011**, *1*, 211–228.
20. Kroman, J. C.; Bratholm, A. GitHub: Calculate RMSD for two XYZ structures. <http://github.com/charnley/rmsd>, **2016**.

- 
21. Aquilante, F.; Gagliardi, L.; Pedersen, T. B.; Lindh, R. Atomic Cholesky Decompositions: A Route to Unbiased Auxiliary Basis Sets for Density Fitting Approximation with Tunable Accuracy and Efficiency. *J. Chem. Phys.* **2009**, 130, 154107.
22. Goodwin, C. A. P.; Ortu, F.; Reta, D.; Chilton, N. F.; Mills, D. P. Molecular magnetic hysteresis at 60 kelvin in dysprosocenium. *Nature* **2017**, 548, 439–442.
23. Jun, J.; Islam, M. A.; Pecoraro, V. L.; Mallah, T.; Berthon, C.; Bolvin, H. Derivation of Lanthanide Series Crystal Field Parameters From First Principles. *Chem. Eur. J.* **2019**, DOI:10.1002/chem.201903141.